Cell

Controlling human organoid symmetry breaking reveals signaling gradients drive segmentation clock waves

Graphical abstract

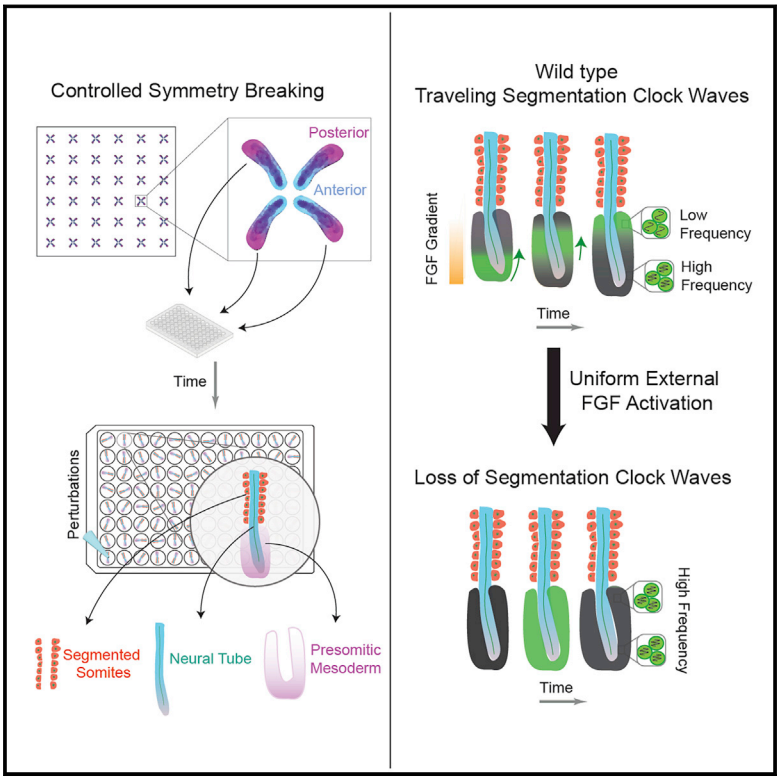

Highlights

- Coupled organoids reproducibly generate neural tube, presomitic mesoderm, and somites
- Organoids display traveling clock waves, sequential segmentation during somitogenesis
- FGF and not WNT pathway determines the position of determination front
- FGF gradient drives traveling waves by modulating the frequency of HES7 oscillations

Authors

Yusuf Ilker Yaman, Sharad Ramanathan

Correspondence

yyaman@g.harvard.edu (Y.I.Y.),
sharad@cgr.harvard.edu (S.R.)

In brief

A robust human stem cell model of axial morphogenesis shows that FGF signaling governs both the dynamics of segmentation clock waves and the somite determination front.

Yaman & Ramanathan, 2023, Cell *186*, 1–15
February 2, 2023
https://doi.org/10.1016/j.cell.2022.12.042

CellPress

Cell

CellPress

Article

Controlling human organoid symmetry breaking reveals signaling gradients drive segmentation clock waves

Yusuf Ilker Yaman[1,3,*] and Sharad Ramanathan[1,2,3,4,*]
[1]John A. Paulson School of Engineering and Applied Sciences, Harvard University, Cambridge, MA 02138, USA
[2]Department of Molecular and Cellular Biology, Harvard University, Cambridge, MA 02138, USA
[3]Department of Stem Cell and Regenerative Biology, Harvard University, Cambridge, MA 02138, USA
[4]Lead contact
*Correspondence: yyaman@g.harvard.edu (Y.I.Y.), sharad@cgr.harvard.edu (S.R.)
https://doi.org/10.1016/j.cell.2022.12.042

SUMMARY

Axial development of mammals involves coordinated morphogenetic events, including axial elongation, somitogenesis, and neural tube formation. To gain insight into the signals controlling the dynamics of human axial morphogenesis, we generated axially elongating organoids by inducing anteroposterior symmetry breaking of spatially coupled epithelial cysts derived from human pluripotent stem cells. Each organoid was composed of a neural tube flanked by presomitic mesoderm sequentially segmented into somites. Periodic activation of the somite differentiation gene MESP2 coincided in space and time with anteriorly traveling segmentation clock waves in the presomitic mesoderm of the organoids, recapitulating critical aspects of somitogenesis. Timed perturbations demonstrated that FGF and WNT signaling play distinct roles in axial elongation and somitogenesis, and that FGF signaling gradients drive segmentation clock waves. By generating and perturbing organoids that robustly recapitulate the architecture of multiple axial tissues in human embryos, this work offers a means to dissect mechanisms underlying human embryogenesis.

INTRODUCTION

The progenitors in the tail bud of the axially elongating mammalian embryo give rise to the posterior neural tube and the flanking presomitic mesoderm (PSM).[1,2] The PSM is further patterned and segmented into somites (Figure 1A), which in turn give rise to the axial skeleton, skeletal muscles, and dorsal dermis,[3] while the posterior neural tube gives rise to the spinal cord.[4] Periodic and sequential segmentation of PSM into somites is controlled by the segmentation clock, which is a complex network of oscillating genes under the control of NOTCH, fibroblast growth factor (FGF), and WNT pathways.[5] The cyclic expression of these genes travels anteriorly through the PSM as a gene expression wave.[6–8] When each such segmentation clock wave reaches the anterior end of the PSM, it initiates the segmentation program of the next presumptive somite pair. Thus, the boundary between the somites and the undifferentiated PSM, called the somite determination front, moves posteriorly with every wave. During development, the embryo must coordinate the dynamics of multiple processes, including axial elongation, PSM generation, anterior movement of the segmentation clock waves in the PSM, posterior movement of the somite determination front, and somite segmentation. FGF and WNT pathways are required for axial elongation[9–11] and the differentiation of axial progenitors into presomitic mesoderm[12] in mouse, chick, and zebrafish. In addition, the position of the somite determination front along the anteroposterior axis is thought to be defined by FGF and WNT signaling gradients in different vertebrates.[9,13–16] However, the mechanisms underlying the anterior movement of segmentation clock waves and the interaction of these waves with the signaling gradients remain unknown.[17]

The challenges in measuring and perturbing the dynamics of mouse embryos *in utero* and the ethical challenge in studying human development necessitate using *in vitro* systems. Recently, oscillating gene expression patterns and the generation of somitic mesoderm have been reported in monolayer cultures of human pluripotent stem cell-derived PSM cells, which is the first evidence for the existence of a segmentation clock in humans.[18–20] In exciting recent work, mouse and human stem cell-derived organoids have been directed to extend axially and generate neural progenitors and somites.[21–23] However, the morphological variability from organoid to organoid and defects in the architecture of the underlying tissues in these *in vitro* systems significantly limit the use of chemical and genetic perturbations to gain mechanistic insight.[24] The ability to generate reproducible and robust organoids that recapitulate human axial development is essential for progress. Furthermore, such organoids will allow dynamic measurements and temporally controlled perturbations in a manner that is impossible *in vivo.*

Please cite this article in press as: Yaman and Ramanathan, Controlling human organoid symmetry breaking reveals signaling gradients drive segmentation clock waves, Cell (2023), https://doi.org/10.1016/j.cell.2022.12.042

Here, we aimed to characterize the dynamics of human axial patterning and morphogenesis to understand how segmentation clock waves interact with signaling gradients. Following the methods developed in a companion manuscript in this issue of *Cell*,[25] we employed a combination of machine learning and bioengineering tools to tune the coupling of human pluripotent stem cell organoids by controlling their spatial arrangement. This enabled us to generate hundreds of *in vitro* organoids simultaneously, each robustly and reproducibly recapitulating the architecture of axial tissues in human embryos. Using single-cell sequencing and computational analysis, we validated the organoids by determining the cell-type composition and the spatial profiles of key transcription factors and signaling molecules along the anteroposterior axis. We demonstrated that the organoids recapitulate the dynamics of axial elongation, anteriorly moving segmentation clock waves, posteriorly moving somite determination front, and somite segmentation. By perturbing the organoids, we showed that FGF signaling gradients drive the anterior propagation of segmentation clock waves while simultaneously controlling the movement of the somite determination front, somite segmentation, and, together with WNT, axial elongation. We finally discuss the implications of these results in the context of the existing models for axial patterning of the somites.

RESULTS

Spatially coupled organoids achieve robust A-P symmetry breaking

To understand human axial development, we aimed to generate hundreds of organoids, each with an axially extending tail bud that generates a single lumen neural tube flanked posteriorly by PSM and anteriorly by somites as seen *in vivo* (Figure 1A). To achieve this desired outcome, we built upon a bioengineering and machine learning framework developed in a companion manuscript to reproducibly break anterior-posterior (A-P) symmetry.[25] We first recapitulated the human epiblast[26] by micropatterning human pluripotent stem cells at random locations on a glass coverslip and folding them into 150-μm diameter cysts composed of a single epithelial layer of pluripotent stem cells enclosing a lumen.[25] To induce differentiation, we exposed the cysts to medium containing WNT agonist CHIR99021 ([CHIR], at concentrations ranging from 2.5 μM to 6 μM) while inhibiting bone morphogenetic protein signaling ([BMP], using LDN193189, 0.5 μM) and transforming growth factor beta signaling ([TGF-β], using A83-01, 0.5 μM). After 48 h, we stained the differentiated organoids for SOX2 and TBXT (Figures 1B and S1A). These markers were chosen to label the SOX2+TBXT + neuromesodermal progenitors (NMP) in the tail bud, SOX2- TBXT + paraxial mesoderm flanking the neural tube posteriorly, and the SOX2+TBXT-cells of the neural tube. In the desired organoid morphology, we expected TBXT to be posteriorly expressed relative to SOX2. We thus scored our organoids using a polarization metric, defined as the distance between the centroid of TBXT + cells and that of SOX2+ cells in each organoid (Figure 1A). The organoids on the random pattern showed a large variability in $\mu^{TBXT/SOX2}_{measured}$ (Figures 1B and 1D). Using the approach in Anand et al., we optimized the spatial arrangement of the differentiating organoids on a coverslip and the CHIR concentration such that each organoid broke A-P symmetry to acquire a large $\mu^{TBXT/SOX2}_{measured}$. This arrangement consisted of 150-μm diameter organoids in groups of four at the vertices of 200 by 200 μm squares (Figures 1C and S1A). After exposure to 4 μM CHIR for 48 h, every organoid broke A-P symmetry and was polarized with low SOX2/high TBXT posteriorly and high SOX2/low TBXT anteriorly (Figures 1C–1E and S1A). To visualize this polarization in live organoids, we used a dual fluorescence reporter HES7:Achilles/MESP2:mCherry iPSC line,[18] allowing us to monitor the polarization of the PSM marker HES7 (Figure 1F).

Polarized organoids with posteriorly localized NMPs generate a single-lumen neural tube flanked by segmented somites

After the initial A-P symmetry breaking at 48 h, randomly selected 96 organoids of the 144 on the same coverslip were removed and cultured individually in low-adhesion 96-well plates in basal media (E6) supplemented with Matrigel, without any signaling molecules or inhibitors. From 72 to 120 h after the start of differentiation, all the organoids that were successfully transferred to the 96-well plate underwent axial elongation (Figures 1H, 1I, and S1C). They also contained a TBXT + SOX2+ NMP population at the posterior tip that was maintained throughout 120 h of differentiation (Figures 1G and S1D). Every organoid showed lateral expression of the somitogenesis marker MESP2 based on mCherry expression (Figure 1H) and displayed anterior to posterior progression of the MESP2+ somite fate (Figures 1H, 1I, and S1C, n = 95).

We next determined the expression patterns of key proteins in these organoids at 120 h through immunostaining. Every organoid had an anteriorly positioned SOX1+ and SOX2+ neural tube with a single lumen and the proper apicobasal polarity as shown by ZO-1 and N-cadherin stains marking the apical tight junctions between epithelial cells (Figures 1J, S1G, and S1H). In each organoid, the neural tube was flanked posteriorly by TBX6+ paraxial mesoderm and anteriorly by the MESP2+ somite cells (Figures 1K and S1E). ZO-1 and N-cadherin expression was localized in multiple foci in the MESP2+ somite region, showing the segmented architecture of somites flanking the anterior neural tube (Figures 1J, S1G, and S1H). Similar to the A-P organization of the developing embryo,[27] the TBX6-expressing domain formed a clear boundary corresponding to the somite determination front, posterior to the MESP2+ cells (Figures 1K, S1E, and S1F). By 120 h of differentiation, the MESP2 expression pattern had resolved into an alternating pattern in each segment as seen *in vivo*,[27–29] indicating that the somites displayed A-P compartmentalization (Figure 1L). These results together demonstrate that our approach robustly achieved the differentiation of pluripotent stem cells into organoids with correctly positioned tail bud, neural tube, and somite structures, capturing key aspects of *in vivo* axial development.

Clustering and diffusion map analysis of axial organoid transcriptome reveals cell types and A-P organization of neural tube and paraxial mesoderm

To explore the cell-type composition of organoids, we performed single-cell RNA sequencing (scRNA-seq) of 11,009 cells obtained from 10 organoids at 120 h (Figure S2A). Clustering and

Please cite this article in press as: Yaman and Ramanathan, Controlling human organoid symmetry breaking reveals signaling gradients drive segmentation clock waves, Cell (2023), https://doi.org/10.1016/j.cell.2022.12.042

CellPress

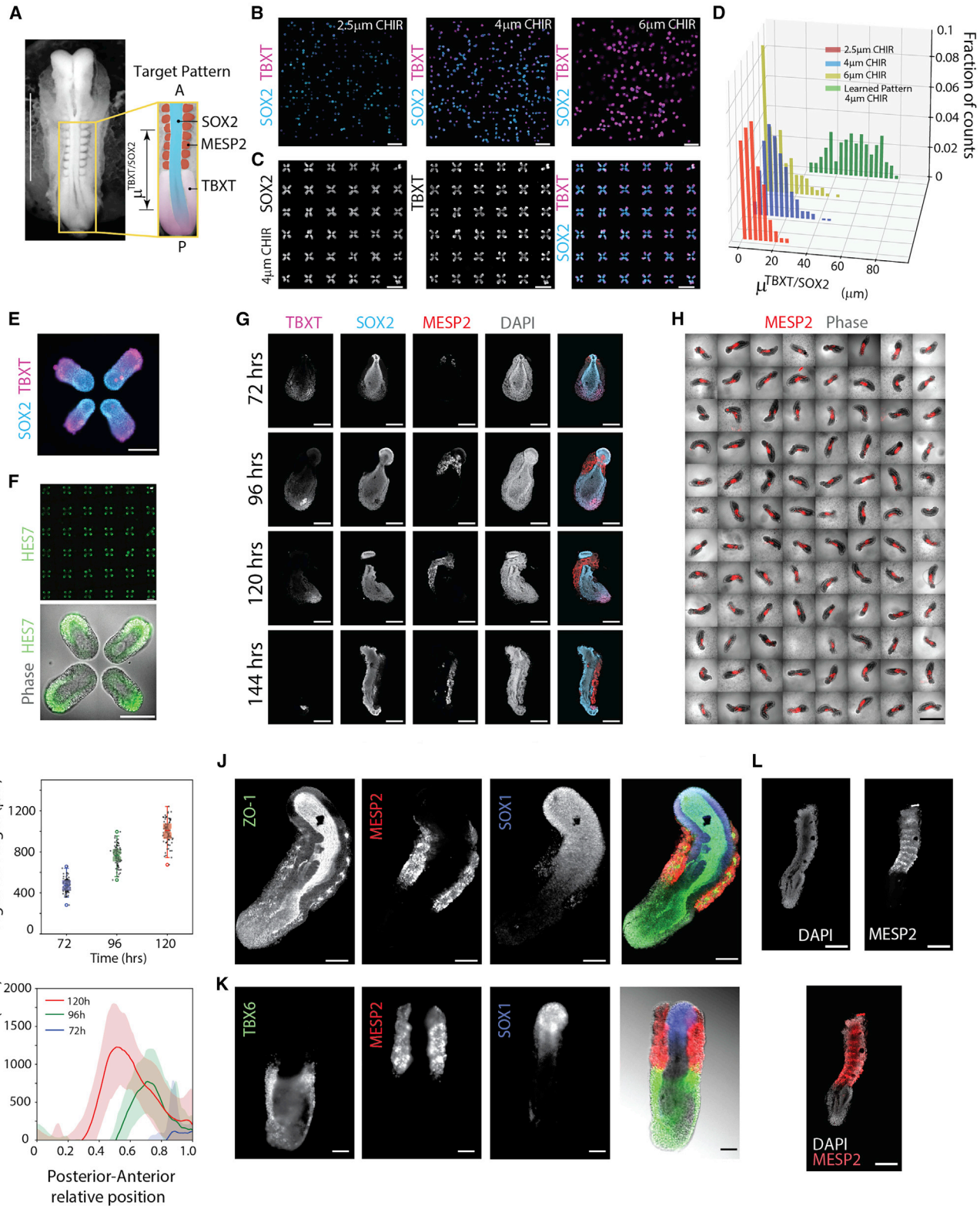

(legend on next page)

Please cite this article in press as: Yaman and Ramanathan, Controlling human organoid symmetry breaking reveals signaling gradients drive segmentation clock waves, Cell (2023), https://doi.org/10.1016/j.cell.2022.12.042

identifying cell types from this data requires measuring the distance between cells in gene expression space. The Euclidean distance in the space of all high-variance genes leads to incorrect clustering and classification.[30] To overcome this challenge, we previously developed and validated an unsupervised statistical method, sparse multimodal decomposition (SMD), to identify the key subset of genes that can be used to determine cell types.[31] Using SMD, we identified 48 key genes with significant *Z* scores from the single-cell data (Figures 2A and S2B). Through hierarchical clustering in this gene subspace, we identified seven cell types in the organoids (Figures 2A, 2B, S2B, and S2C). The first cluster co-expressed TBXT and SOX2, indicating a NMP identity.[1] The second cluster, consisting of SOX2+TBXT-cells, co-expressed tail bud genes HOXA10, CDX2, and NKX1-2, consistent with a pre-neural tube identity.[32] A third cluster possessed a neural progenitor identity, expressing neural markers SOX1, PAX6, HES5, and IRX3 along with high levels of SOX2.[4] Three additional clusters were associated with paraxial mesodermal identity. These included a PSM-like cell cluster expressing TBX6, MSGN1, and HES7; an early somite cell cluster expressing MEOX1, TCF15, and RIPPLY1; and a mature somite cell cluster expressing PAX3, TWIST1, and FST.[33] Lastly, we identified a small number of notochord cells expressing SHH, NOTO, and high levels of TBXT.[34,35]

To map the spatial distribution of neural and mesodermal lineages present in organoids from scRNA-seq data, we constructed a diffusion map[36] in the subspace of genes identified by SMD (Figure 2B). We previously showed that such a map could recapitulate the spatial ordering of cells along the A-P axis, allowing the inference of spatial profiles of gene expression.[25] We plotted the expression levels of genes arranged in order of the position of their peak expression level along the inferred posterior to anterior axis in both the neural and mesodermal tissues (Figures 2C and 2D). In the mesodermal cells, genes expressed in the tail bud progenitors (TBXT, CDX1, CDX2, CDX4, LIN28A, HOXA10, HOXC10) peak most posteriorly, followed by the marker genes of PSM (TBX6, DLL3, DLL1, MSGN1), followed by the somite determination front marker MESP2, then early somite markers (MEOX1, RIPPLY1, TCF15), and finally mature somite markers (SIX1, PAX3, ALCAM)[37] (Figures 2C, 2E, and S2D). Along the neural lineage, cells closest to the NMP expressed pre-neural tube markers CDX2, MSX1, and NKX1-2 (Figures 2D and S2D). On the other hand, anteriorly positioned cells expressed higher levels of neural progenitor markers SOX1, PAX6, OLIG3, and IRX2, together with higher levels of SOX2[4] (Figures 2D, 2E, and S2D). We verified the inferred A-P expression profiles of the marker genes by MESP2:mCherry reporter expression and immunostaining against TBXT, TBX6 (Figures S1D and S1E), and for mesodermal cells and SOX2, SOX1 and PAX6 for neural cells (Figures S2H and S1D).

Inferring the anteroposterior profiles of WNT, FGF, RA, NOTCH, and BMP signaling pathway components in the mesodermal and neural tissues

We next tested whether our organoids recapitulated the anteroposterior expression gradients of WNT, FGF, retinoic acid (RA), and NOTCH signals and their targets as observed *in vivo* in

Figure 1. Elongating axial organoids generates neural tube with a single lumen flanked anteriorly by segmented somites and posteriorly by presomitic mesoderm

(A) Left: micrograph of Carnegie Stage 10 human embryo, Kyoto Collection. Right: target pattern with expression profiles of MESP2, TBXT, and SOX2 colored and overlayed on the posterior part of the human embryo micrograph. Scale bar, 1 mm.

(B) Randomly positioned organoids on a coverslip, each consisting of a single epithelial layer of cells enclosing a single lumen, treated with BMP inhibitor LDN193189 (0.5 μM), TGFβ inhibitor A83-10 (0.5 μM), and WNT agonist CHIR99021 (left to right: 2.5 μM, 4 μM, 6 μM) for 48 h stained for TBXT and SOX2. Scale bar, 1 mm.

(C) Organoids micropatterned in groups of four on the vertices of a square after 48 h of differentiation, stained for TBXT (left) and SOX2 (middle), color combined (right). Scale bars, 1 mm.

(D) Histogram showing the distribution of organoid polarization metric on random arrays for each CHIR concentration and on the vertices of squares at 4 μM CHIR concentration.

(E) Magnified image of one set of four organoids on the vertices of a square at 48 h of differentiation stained for TBXT and SOX2. Scale bar, 200 μm.

(F) Organoids micropatterned in groups of four on the vertices of a square after 48 h of differentiation with live HES7 reporter signal (green) shown for a full array (top); magnified and overlayed on the phase image for one set of four organoids (bottom). One hundred percent of the organoids on coverslips show polarized expression HES7. Scale bars: 1 mm top, 200 μm bottom.

(G) Confocal sections of representative organoids with MESP2:mCherry reporter on consecutive days of differentiation (72 h, 96 h, 120 h, 144 h) stained for TBXT, and SOX2. TBXT and SOX2 co-expressing NMPs reside at the posterior tip. MESP2 progression starts anteriorly and moves toward the tip during 144 h of differentiation. Scale bars, 200 μm.

(H) Phase contrast images overlayed with MESP2:mCherry signal in live organoids randomly selected from 144 organoids grown on the same coverslip and transferred to a 96-well low-adhesion plate at 120 h of differentiation. All organoids show elongated morphology and lateral MESP2:mCherry expression. Scale bar, 1 mm.

(I) Top: quantification of elongation. Boxplot of length of the organoids on 72 h, 96 h, and 120 h of differentiation. Dots are individual data points. Center line, median; box, interquartile range; whiskers, range not including outliers; empty circles, outliers. n = 95 independent biological replicates. Bottom: quantification of MESP2 reporter expression along the anteroposterior axis of the organoids on 72 h, 96 h, and 120 h of differentiation. Solid lines, means; shaded area, std; AU, arbitrary units. n = 95 independent biological replicates.

(J) Confocal section of a representative organoid with MESP2:mCherry reporter stained for tight junction marker ZO-1 and SOX1 at 120 h of differentiation. Scale bars, 100 μm.

(K) Epifluorescence image of a representative organoid with MESP2:mCherry reporter stained for paraxial mesoderm marker TBX6 and neural marker SOX1 at 120 h of differentiation. Color combined fluorescence images overlayed on phase contrast image (rightmost image). Scale bars, 100 μm.

(L) Confocal section of a representative organoid showing alternating expression of MESP2 reporter on 120 h of differentiation, stained for DAPI. Scale bar, 200 μm.

See also Figure S1.

Please cite this article in press as: Yaman and Ramanathan, Controlling human organoid symmetry breaking reveals signaling gradients drive segmentation clock waves, Cell (2023), https://doi.org/10.1016/j.cell.2022.12.042

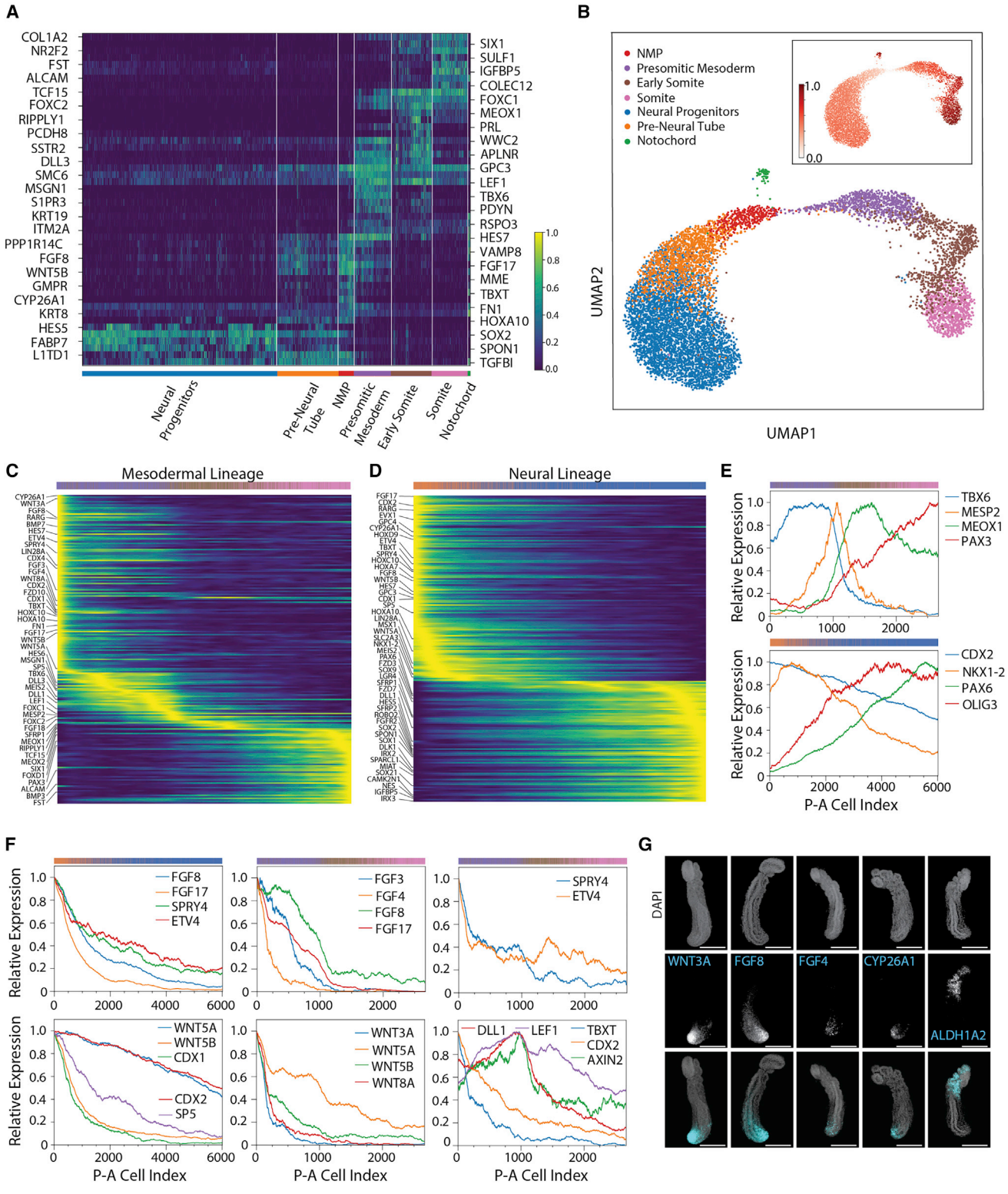

Figure 2. Anteroposterior organization of cell types and gene expression profiles inferred from single-cell RNA-seq

(A) Normalized gene expression heatmap of 11,009 cells from 120 h organoids, hierarchically clustered in the subspace of 48 genes identified by sparse multimodal decomposition. The inferred identities of the 7 clusters are labeled below.

(legend continued on next page)

Please cite this article in press as: Yaman and Ramanathan, Controlling human organoid symmetry breaking reveals signaling gradients drive segmentation clock waves, Cell (2023), https://doi.org/10.1016/j.cell.2022.12.042

mouse, chick, and zebrafish embryos.[4,38] The expression profile of the detected FGF ligands in neural cells (FGF8, FGF17; Figure 2F) and mesodermal cells (FGF3, FGF4, FGF8, FGF17; Figure 2F) were localized most posteriorly in each lineage. FGF receptors were differentially expressed between the mesoderm and neural tissues, with FGFR1 expressed throughout the mesoderm and FGFR2 showing monotonically increasing levels from posterior to anterior in the neural tube (Figure S2E). In both tissues, FGF target genes SPRY4 and ETV4 were upregulated posteriorly (Figure 2F), consistent with the role of FGF in maintaining the axial progenitor state in the tail bud of the mouse embryo.[15,39]

Like FGF, all detected WNT ligands showed a posterior to anterior graded expression. Although both canonical (WNT3A, WNT8A) and noncanonical (WNT5A, WNT5B) WNT ligands were expressed in the mesodermal tissue (Figure 2F), only noncanonical (WNT5A, WNT5B) WNT ligands showed expression in the neural tissue (Figure 2F). The WNT ligand expression gradient was opposed by an expression gradient of secreted WNT inhibitors SFRP1 and SFRP2 in both mesoderm and neural lineages (Figure S2F). WNT targets (CDX2, CDX1, SP5) showed a posteriorly restricted expression pattern in the neural tissue similar to that of WNT ligands (Figure 2F). In the mesodermal tissue, one class of WNT targets (TBXT, CDX2, CDX4), was highly expressed at the posterior end of the tissue and downregulated anteriorly. The second class of targets (AXIN2, DLL1) and the WNT transcriptional mediator LEF1 showed peak expression at the anterior end of the PSM closest to the somite determination front (Figure 2F).

RA signaling is important in mouse embryos for the fate specification of NMPs, differentiation of PSM, and the patterning of the neural tube.[1] We observed that in our organoids, while the retinoic acid receptor gamma (RARG) was expressed throughout the neural and mesodermal tissues, the RA synthesis gene ALDH1A2 was expressed only in the somites anteriorly (Figure S2G). Anterior RA secretion from somites combined with the posterior expression of the RA degradation enzyme CYP26A1 (Figure S2G) is consistent with an A-P RA gradient. Anterior upregulation of transcription factor PAX6 known to be downstream of retinoic acid signaling[40] suggested that the neural tube was patterned by RA secreted by the flanking somites. Consistent with this, immunostaining showed upregulation of PAX6 protein in the section of the neural tube in proximity to the somites (Figure S2H).

Next, we investigated the NOTCH signaling pathway, a key component in regulating periodic somite segmentation and neurogenesis.[41,42] In the mesodermal lineage, both NOTCH pathway ligands (DLL1, DLL3), receptor (NOTCH1), and targets (HES6, HES7) were highly expressed in the PSM and downregulated anterior to the somite determination front (Figure S2I). Although the NOTCH receptor expression levels were very low in the neural tissue, NOTCH ligand DLL1 and NOTCH target gene HES5 were upregulated in the neural progenitors anteriorly, suggesting the initiation of neurogenesis (Figure S2I).

To validate the computationally inferred anteroposterior expression profiles of genes involved in signaling, we performed *in situ* hybridization chain reaction (HCR) for WNT3A, FGF8, FGF4, CYP26A1, and ALDH1A2 on organoids upon 120 h of differentiation (Figure 2G). Consistent with the inferred profiles, WNT3A (n = 3), FGF8 (n = 5), FGF4 (n = 3), and CYP26A1 (n = 3) had posterior to anterior graded expression, whereas ALDH1A2 (n = 3) expression was localized anteriorly at somites. Further, to determine whether the anteroposterior expression gradients of WNT and FGF ligands were reflected in the signaling pathway activity, we immunostained organoids for diphosphorylated ERK (dpERK) and β-catenin (Figures S2L and S2M). Nuclear segmentation and quantification of dpERK and β-catenin signals showed that the signaling activity for both FGF and WNT pathways was high at the posterior tip and gradually decreased anteriorly (Figures S2L and S2M). In total, our human organoid model shows anteroposterior expression gradients of WNT, FGF, RA, and NOTCH signals and targets consistent with *in vivo* observations in mouse, chick, and zebrafish embryos.

The dorsoventral patterning of somites and the neural tube is regulated by opposing gradients of BMPs secreted by surface ectoderm, roof plate, and somites, and SHH secreted by the notochord and floor plate.[43] Though our organoids lack roof plate and floor plate cell types, BMP7 was expressed by NMPs and the posterior PSM, and BMP4 and BMP3 were expressed by somites (Figure S2J). The presence of dorsalizing signals was consistent with acquiring a dorsal identity by both neural progenitor cells and somite cells. Neural progenitor cells expressed dorsal neural tube markers MSX1, OLIG3, IRX3, and PAX3,[44] and somite cells expressed a dermomyotome marker PAX3,[33] seen only dorsally in somites *in vivo*. In contrast, the ventral somite marker PAX1[45] was not expressed in any cells

(B) Uniform manifold approximation and projection (UMAP) plot generated in the subspace of genes identified by sparse multimodal decomposition. Cells are colored by their cluster identity (see legend for color code, same as in A). Inset shows the UMAP plot colored by inferred anteroposterior positions of cells obtained by diffusion mapping (see STAR Methods).

(C and D) Heatmap of top 200 differentially expressed genes (y axis) in the mesodermal (C) cell clusters (presomitic mesoderm, early somite, and somite) and neural (D) cell clusters (pre-neural tube and neural progenitors) in cells (x axis) ordered according to their inferred anteroposterior positions. Genes are ordered based on the position of their peak expression on the inferred A-P axis. Color bars on the top of heatmaps represent the cluster identity of the individual cells (same color code as in A).

(E and F) Normalized posterior-anterior (P-A) gene expression profiles for marker genes of mesodermal (E, top) and neural cell clusters (E, bottom); FGF pathway ligands and targets (F, top left), WNT pathway ligands and targets (F, bottom left) in neural clusters; FGF pathway ligands (F, top middle) and targets (F, top right), WNT pathway ligands (F, bottom middle) and targets (F, bottom right) in mesodermal cell clusters. Bars on the top of each plot represent cells at that position along the inferred P-A axis, colored by their cluster identity (same color code as in A).

(G) Confocal images of organoids stained for WNT3A, FGF8, FGF4, CYP26A1, and ALDH1A2 using HCR (columns from left to right). WNT3A, FGF8, FGF4, and CYP26A1 are localized posteriorly and have a graded expression on the anteroposterior axis. ALDH1A2 is localized anteriorly, expressed only in somite cells. Scale bar, 200 μm.

See also Figures S2 and S3.

Please cite this article in press as: Yaman and Ramanathan, Controlling human organoid symmetry breaking reveals signaling gradients drive segmentation clock waves, Cell (2023), https://doi.org/10.1016/j.cell.2022.12.042

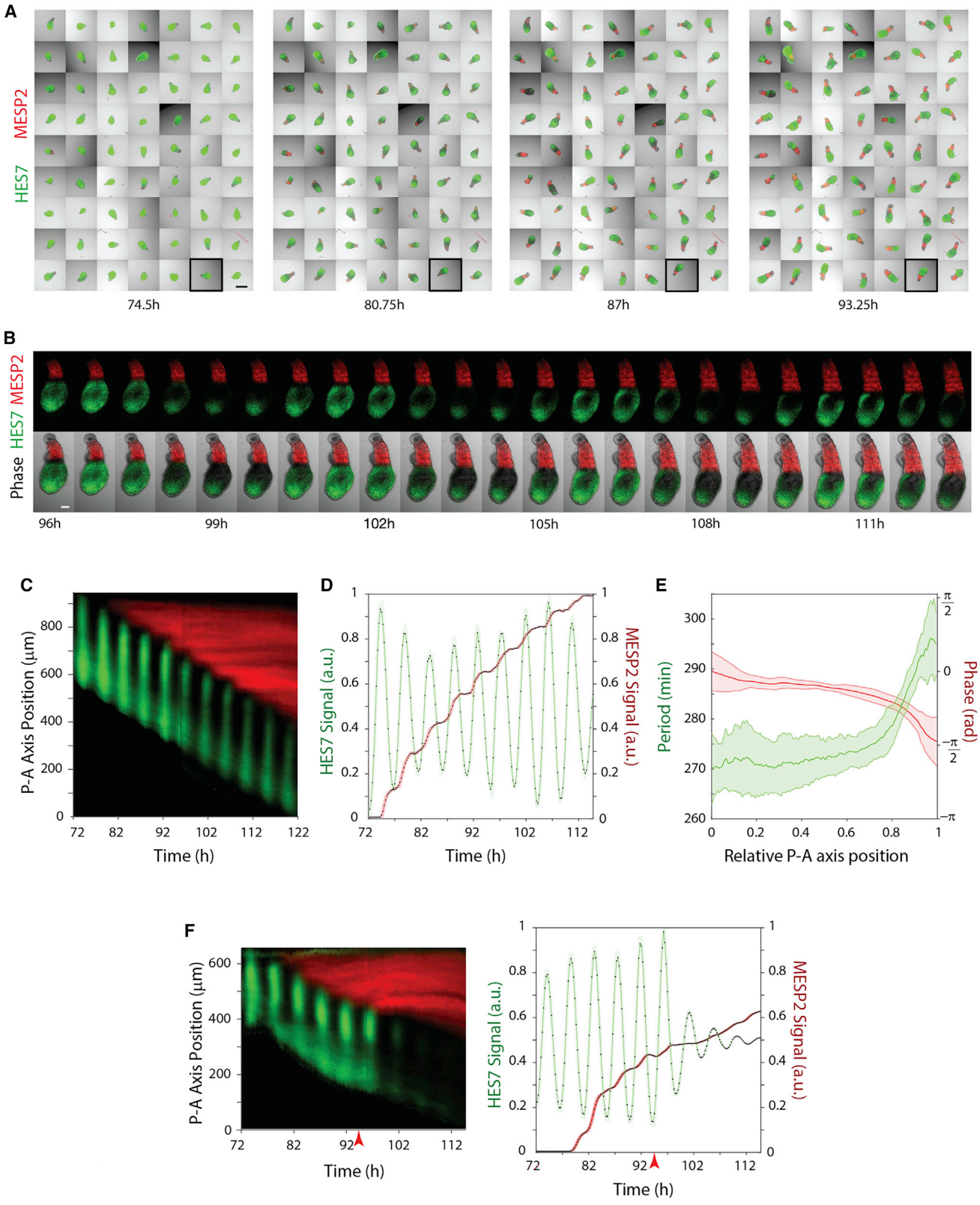

(legend on next page)

Please cite this article in press as: Yaman and Ramanathan, Controlling human organoid symmetry breaking reveals signaling gradients drive segmentation clock waves, Cell (2023), https://doi.org/10.1016/j.cell.2022.12.042

(Figure S2J), consistent with the lack of SHH expression by cells. We also observed the expression of a neural crest marker SOX9 and the epithelial-to-mesenchymal transition gene SNAI2 in a subset of neural progenitors (Figure S2K). Thus, in the absence of SHH, tail bud progenitors generated only dorsal neural and mesodermal cell types, possibly through the dorsalizing effect of BMPs secreted by mesodermal cells.

We compared our scRNA-seq data with a previously published scRNA-seq data obtained from E9.5 mouse embryo tail bud.[18] The cell types identified in our axial organoid model were consistent with their *in vivo* counterparts (see STAR Methods and Figures S3A–S3E).

Axial organoids show sequential somite segmentation coordinated with traveling segmentation clock waves

Given that the morphology, composition, and signaling profiles of 120-hour-old organoids were consistent with those of mammalian embryos, we next measured the dynamics of somitogenesis. We tested whether the organoids showed anteriorly propagating segmentation clock waves in the PSM and a coordinated posteriorly propagating somite determination front. We performed time-lapse imaging of organoids built with the dual reporter HES7-Achilles/MESP2-mCherry iPSC line. After 72 h of differentiation, when the first somite cells appeared at the anterior end, we transferred organoids to individual wells of a glass-bottom 96-well plate for imaging. Each organoid showed oscillating HES7 expression and posteriorly propagating MESP2 expression (Figures 3A, 3B, S4B, and Videos S1 and S2). Quantification of Achilles and mCherry signals showed that the MESP2+ region expanded in a step-like fashion. Each step in the MESP2 profile coincided with a peak of HES7 oscillations at the anterior end of the PSM, indicating that the timing of somite differentiation is coordinated with the segmentation clock wave in the axial organoids (Figures 3C, 3D, and S4B). Characterizing the HES7 oscillations along the A-P axis showed transient dynamics with almost synchronous oscillations throughout the PSM when the first somites appear around 72 h. This is consistent with recent reports in mouse.[46] By 96 h of differentiation, a global phase gradient was established in 91% of the organoids (n = 53). In these organoids, oscillations at the anterior tip lagged the posterior tip, resulting in anteriorly moving traveling waves (Figure S4A). By 115 h of differentiation, all organoids showed anteriorly propagating traveling waves with $\pi/2$ radians phase difference between posterior and anterior PSM on average (n = 14; Figures 3E, S4A, and S4C). We also found that the oscillations were faster posteriorly compared to the anterior, with a period of 4.5 h at the posterior tip and around 5 h at the anterior PSM. (Figure 3E). In mouse, chick, and zebrafish embryos, the NOTCH pathway has been implicated in driving intracellular gene expression oscillations and somite segmentation.[5,27,41] In line with *in vivo* studies,[47,48] inhibition of NOTCH signaling through DAPT (25 μM) treatment resulted in the downregulation of HES7 oscillation amplitude and the impairment of MESP2 progression consistent with MESP2 being a NOTCH target gene (Figures 3F, S4D, and Video S2). Thus, our *in vitro* organoid model recapitulates traveling segmentation clock waves and sequential somite segmentation as observed *in vivo*.

FGF and WNT pathways have complementary roles in axial elongation, movement of the somite determination front, and somite segmentation

In our organoids, WNT inhibition using the WNT secretion inhibitor IWP-2 (2 μM) added during somitogenesis resulted in truncated organoids with truncated PSM (Figures 4A, 4B, and S5A). However, we did not observe an effect of WNT inhibition on the movement of the somite determination front. We continued to see step-like segmentation with segment sizes similar to control organoids (Figures 4C, S5A, and Video S2). Consistently, when ectopic WNT activation was uniformly stimulated by CHIR (3 μM) addition at 96 h of differentiation, organoids were elongated and developed a longer PSM compared to controls (Figures 4D, S5B, and S5C). These organoids continued to show step-like MESP2 progression without a significant change in somitic mesoderm length or defects in segmentation compared to control organoids (Figures 4D–4F, S5B, S5C, and S5E). These results show that the WNT pathway directly promotes axial elongation and has little effect on the progression of the determination front or somite segmentation.

Conversely, experiments in mouse have indicated that WNT plays a role in defining the position of the determination front.[14] These results were obtained in mice through β-catenin deletion or stabilization. Unlike experiments in organoids or zebrafish,[49,50] where the perturbation can be carefully timed, the effects of these

Figure 3. Dynamics of somitogenesis and NOTCH gene expression waves in the organoids

(A) Stills from time-lapse imaging of organoids (at 74.5 h, 80.75 h, 87 h, and 93.25 h after onset of differentiation) with HES7 (green) and MESP2 (red) expression reporters. All organoids show oscillating HES7 expression and posteriorly propagating MESP2+ somite determination front. Scale bars, 500 μm.

(B) Stills from time-lapse imaging of the organoid are highlighted with a black box in (A) from 96 h to 112.5 h. Organoid shows anteriorly propagating HES7 (green) expression waves and posteriorly propagating MESP2 (red) somite determination front. Time interval between consecutive images is 45 min. Scale bar, 100 μm.

(C) Representative kymograph showing the dynamics of HES7 (green) and MESP2 (red) expression along the anteroposterior axis of organoids from 72 h to 122 h of differentiation. Data collected every 15 min.

(D) HES7 (green) expression at the most anterior tip of the presomitic mesoderm and the length of the MESP2 (red)-expressing region of a representative organoid over time. Data collected every 15 min. Thicker lines show the moving average with a window size of 3 time points, and shaded areas show moving SD with a window size of 3 time points. Black dots represent each data point. AU, arbitrary units.

(E) Plot showing period (left axis, green) and phase (right axis, red) of the oscillations along the anteroposterior axis of presomitic mesoderm of organoids. Lines represent mean and shaded area represent SD over n = 14 biologically independent replicates.

(F) Left: representative kymograph showing the dynamics of HES7 (green) and MESP2 (red) expression along the anteroposterior axis of organoids from 72 h to 114 h of differentiation upon NOTCH inhibition using DAPT. Right: HES7 (green) expression at the most anterior tip of the presomitic mesoderm and the length of the MESP2 (red)-expressing region of a representative organoid over time upon NOTCH inhibition. Data collected every 15 min for both plots. Thicker lines show the moving average with a window size of 3 time points, and shaded areas show moving SD with a window size of 3 time points. Black dots represent each data point. AU, arbitrary units. Red arrow indicates time of DAPT addition.

See also Figure S4 and Videos S1 and S2.

Please cite this article in press as: Yaman and Ramanathan, Controlling human organoid symmetry breaking reveals signaling gradients drive segmentation clock waves, Cell (2023), https://doi.org/10.1016/j.cell.2022.12.042

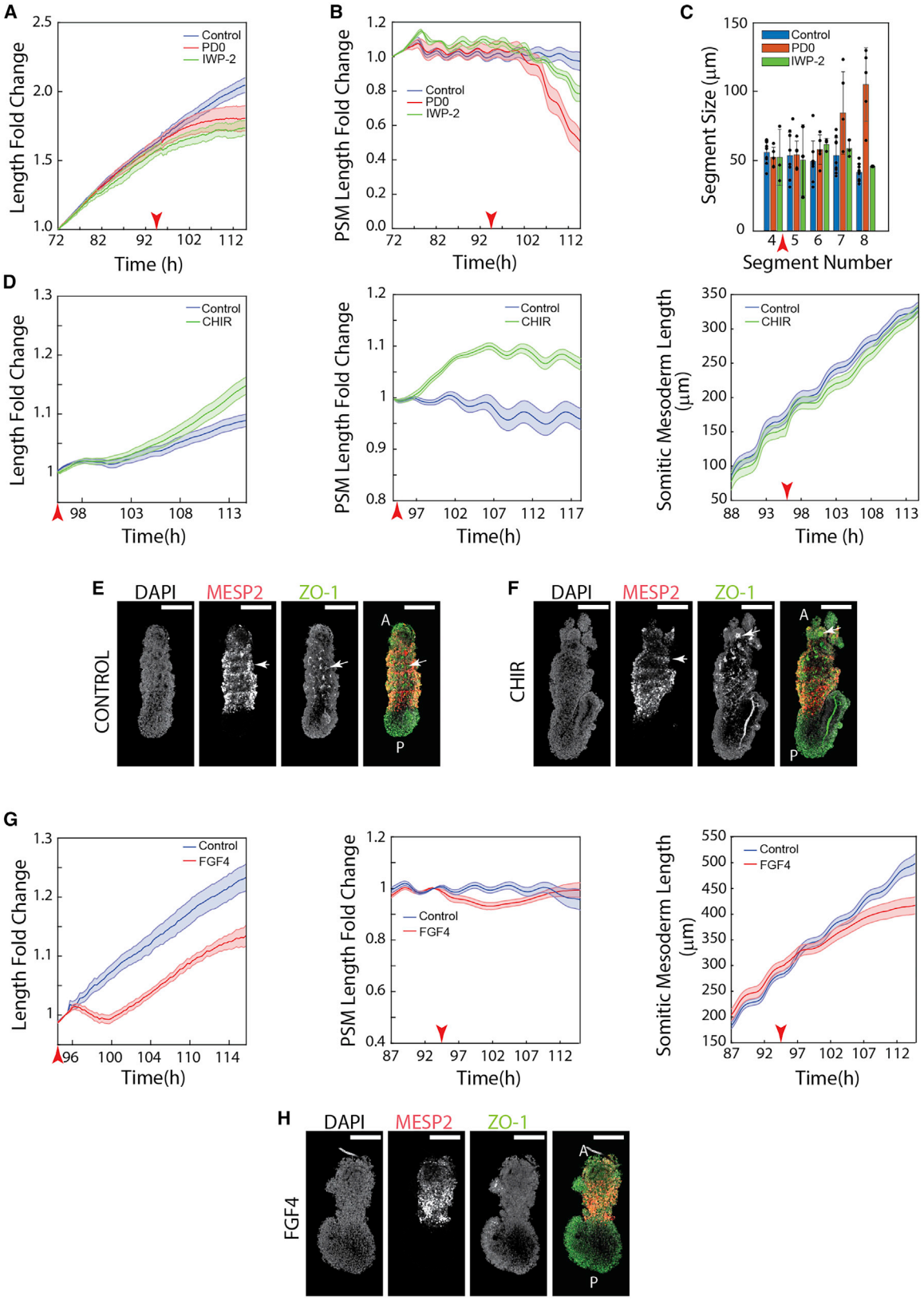

(legend on next page)

Please cite this article in press as: Yaman and Ramanathan, Controlling human organoid symmetry breaking reveals signaling gradients drive segmentation clock waves, Cell (2023), https://doi.org/10.1016/j.cell.2022.12.042

mutations last throughout development, making it difficult to distinguish direct from indirect effects. Indeed, levels of FGF ligand and signaling activity were also significantly affected in these mutants, making it difficult to disentangle the effects of WNT perturbations from the downstream effects through FGF. Therefore, we next tested the role of FGF signaling in axial morphogenesis.

Consistent with studies in chick[13] and zebrafish[51] embryos, FGF inhibition in the organoids using FGF/ERK inhibitor PD0325901 (1 μM) led to truncation, with both the total organoid length and PSM length being shorter than control (Figures 4A, 4B, and S5A). FGF inhibition further led to an accelerating somite determination front propagation, and somite segments were about twice as large as control organoids (Figures 4C, S5A, and Video S2). To observe the effects of FGF activation during somitogenesis, we exposed organoids to FGF4 (100 ng/mL) ligand at 96 h of differentiation. Uniform FGF4 treatment transiently decreased the size of the PSM. The truncation of the organoid compared to control is eventually due to the shortening of the somitic mesoderm. This suggests that a gradient of FGF activity is required for elongation, consistent with the literature.[9,11,52–54] (Figures 4G and S5D). FGF4-treated organoids had a decelerated determination front progression (Figure 4G) and disrupted somite segmentation, as seen by the lack of ZO-1 foci or segments in the perturbed organoids (Figures 4H and S5E). By performing β-catenin and dpERK immunostaining on the organoids treated with CHIR and FGF4, we validated that there was no cross-activation between WNT and FGF pathways after exposure for one oscillation period (4.5 h) (Figures S5F, S5G, and S5H).

These results indicate that although both FGF and WNT pathways are important for the axial elongation of both the neural tube[25] and the mesoderm, the FGF pathway additionally plays a direct role in the definition of the somite determination front and the segmentation of the somites.

FGF4 gradients are required for the propagation of segmentation clock waves

How waves of gene expression travel anteriorly along the PSM remains unknown.[17] Furthermore, we do not know how the waves interact with the FGF and WNT signaling gradients. To determine if diffusible signaling gradients played a role in the propagation of segmentation clock waves, we wanted to place isolated colonies of PSM cells at a distance from each other to determine whether they could still communicate and mutually coordinate their segmentation clock oscillations through diffusive signals. Our logic was that if, in any configuration of these colonies were not physically in contact and we could see coherent wave propagation across the colonies, it would suggest a role for diffusive molecules in the spatial coordination of the segmentation clock. We, therefore, performed the experiments for different spatial configurations of colonies, from those with uniform spacing between the colonies to those with a gradient of colony density. To achieve this, we micropatterned pluripotent stem cell colonies in proximity to each other on a coverslip and constrained colony expansion and cell migration by passivating the coverslip surface (Figures 5A, S6A, and S6B). The colonies could not touch each other, preventing communication between colonies through juxtacrine signaling (such as through NOTCH or YAP). By treating cells with CHIR and LDN for 48 h, we differentiated colonies to a PSM identity. At the end of 48 h, we replaced differentiation media with basal media and recorded HES7 oscillations (Figures 5A and S6A). If diffusible signals did not play a role in generating traveling waves, we expected not to see a phase gradient across the colonies and, concomitantly, no propagation of NOTCH activity waves sweeping coherently across the colonies. In uniformly spaced colonies, time-lapse imaging revealed that the HES7 oscillations were synchronous (Figure S6F). Contrarily, HES7 oscillations were spatially coordinated between the microprinted colonies in the patterns that had a radial density gradient (intercolony distance increases with the distance from the center), and a phase gradient of HES7 oscillations was established, resulting in HES7 waves propagating from colonies at the edge to those in the center of the pattern (Figures 5A–5C, S6A, and Video S3). These results show that when colonies that are not in contact are arranged appropriately in space, their oscillation dynamics are coupled, leading to waves that travel across the colonies. Thus, diffusible signals could be important for the propagation of segmentation clock waves.

We, therefore, investigated whether FGF and WNT signaling could modulate the propagation of the measured HES7 waves in organoids. We observed that FGF inhibition resulted in the downregulation of the amplitude of HES7 oscillations. In

Figure 4. FGF drives somite determination front propagation and somite segmentation, while WNT drives axial elongation

(A and B) Length fold change (A) and presomitic mesoderm length fold change (B) of organoids treated with PD0325901 (1 μM, n = 5, red), IWP-2 (2 μM, n = 4), and unperturbed control (n = 13, blue) over time. Red arrow shows the time point of administration of PD0325901 and IWP-2 for the perturbed organoids. Solid lines, mean; shaded areas, SE.

(C) Bar graph of somite segment sizes in organoids treated with PD0325901 (1 μM, n = 5), IWP-2 (2 μM, n = 4), and unperturbed control (n = 9). Bars represent the mean; whiskers represent the SD. Black dots represent individual organoids.

(D) Length fold change (left), presomitic mesoderm length fold change (middle), and somitic mesoderm length (right) as a function of time in organoids treated CHIR (n = 16, green) and unperturbed control (n = 16, blue). Red arrow shows the time point of administration of CHIR for the perturbed organoids. Solid lines, mean; shaded areas, SE.

(E and F) Confocal images of control (E) and CHIR treated (F) Typical images of organoids stained for DAPI, epithelial marker ZO-1, and somite marker MESP2 show MESP2-expression pattern resolved into an alternating pattern in each segment (one segment marked with white arrow) and segmented epithelial somites (ZO-1 puncta in one individual somite marked with white arrow). The CHIR-treated organoid is substantially longer than control. Scale bar, 200 μm.

(G) Length fold change (left), presomitic mesoderm length fold change (middle), somitic mesoderm length (right) as a function of time in organoids treated with FGF4 (n = 9, red) and unperturbed control (n = 13, blue). Red arrow shows the time point of administration of FGF4 for the perturbed organoids. Solid lines, mean; shaded areas, SE.

(H) Typical image of an FGF4-treated organoid stained for DAPI, epithelial marker ZO-1, and somite marker MESP2. In contrast with control organoids in (E), FGF4-treated organoids do not show segmentation and no ZO-1 puncta associated with epithelial somites. Scale bar, 200 μm.

See also Figure S5 and Video S2.

Please cite this article in press as: Yaman and Ramanathan, Controlling human organoid symmetry breaking reveals signaling gradients drive segmentation clock waves, Cell (2023), https://doi.org/10.1016/j.cell.2022.12.042

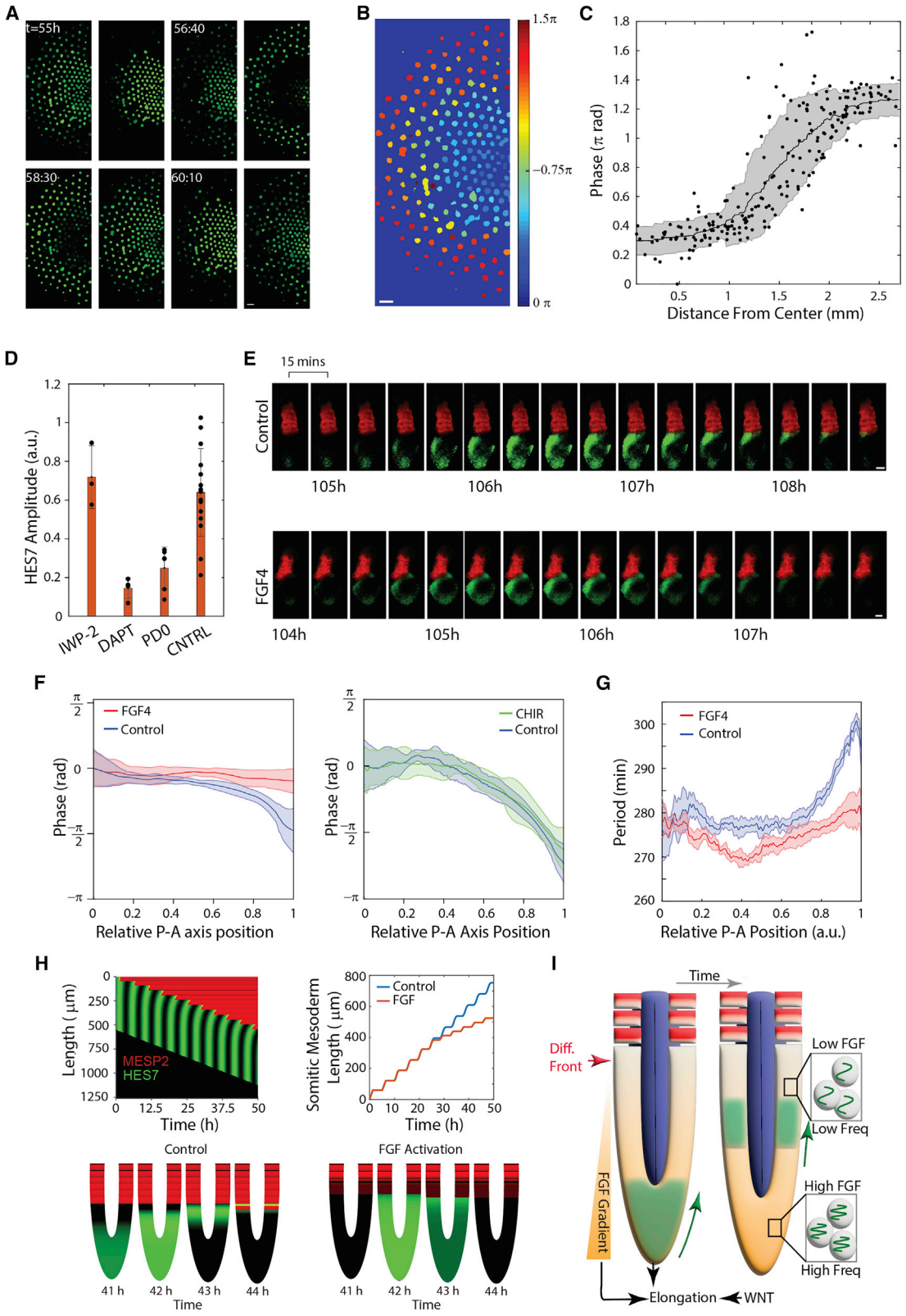

(legend on next page)

Please cite this article in press as: Yaman and Ramanathan, Controlling human organoid symmetry breaking reveals signaling gradients drive segmentation clock waves, Cell (2023), https://doi.org/10.1016/j.cell.2022.12.042

contrast, WNT inhibition did not affect the oscillations (Figure 5D), indicating that the FGF pathway is not only involved in defining the somite determination front and regulating somite segmentation but also in regulating the segmentation clock. We next uniformly activated FGF and WNT pathways in organoids. Time-lapse imaging of organoids revealed that uniformly activating the WNT pathway by adding CHIR did not affect the phase gradient along the A-P axis compared to the control organoids (Figures 5E, 5F, S6C, S6D, and Video S4), showing that the WNT pathway has no direct effects on the dynamics of the segmentation clock. Treating organoids with FGF4 ligand resulted in synchronization of the oscillations throughout the A-P axis and loss of the traveling waves. In contrast, in control organoids, the segmentation clock waves propagated anteriorly through the PSM (Figures 5E, 5F, S6E, and Video S4). Further, FGF4 addition accelerated the oscillations anteriorly, causing anterior and posterior PSM to oscillate with the same period (Figure 5G). Similarly, adding FGF4 to microprinted colonies accelerated oscillations and abolished the traveling waves (Figure S6G). Thus, we concluded that the FGF signaling gradient drives the propagation of segmentation clock waves during human somitogenesis through frequency modulation.

DISCUSSION

In physical systems that break symmetry, coupling the underlying degrees of freedom can substantially reduce the entropy of the broken symmetry state. Demonstrating the power of the approach developed in Anand et al.,[25] our study shows that by similarly coupling organoids, one can reduce the entropy of the broken symmetry state to obtain robust differentiation. The resulting axial organoids recapitulate critical aspects of axial development, including axial elongation, single-lumen neural tube formation, traveling segmentation clock waves, and sequential somite segmentation. These organoids allow us to image and deliver perturbations with temporal precision and at timescales corresponding to the clock oscillation times to extract mechanistic insight. Such an ability will enable us to study mammalian, and specifically human, axial development and associated diseases.

The accessibility of the organoids allowed live imaging, which is challenging *in vivo* in mouse, and impossible in human. Interpreting the effects of *in vivo* genetic perturbations is also challenging as the readouts of these perturbations are often indirect. In contrast, timed perturbations and simultaneous measurements of signaling pathway activity are easily achieved in organoid systems. In conjunction with the reproducibility of our organoids, such an ability is essential for achieving the reported results. Together, the experiments enabled us to obtain three significant insights about axial patterning and morphogenesis. First, we showed that WNT and FGF pathways together drive axial elongation. The absence of either of these signaling pathways leads to axis truncation. Moreover, unlike the WNT pathway, uniform activation of the FGF pathway also leads to axis truncation, highlighting the requirement of an FGF gradient for axial elongation. Second, by observing the immediate changes in determination front position upon temporally controlled inhibition of the FGF and WNT pathways, we could disentangle the roles of these two pathways in axial extension and somite patterning. We showed that the position of the determination front is determined solely by FGF and not by WNT signal. Third, we showed that the FGF signaling gradient along the A-P axis drives segmentation clock waves by modulating the period of the NOTCH oscillations at the cellular level. Posterior to anterior FGF activity gradient thus generates a frequency and phase gradient along this axis, leading to anteriorly traveling segmentation clock waves. Consequently, uniform activation of the

Figure 5. FGF gradient is required for HES7 traveling expression waves and somite segmentation

(A) Stills from time-lapse imaging PSM colonies on microcontact printed arrays with HES7 expression reporter. Detrended HES7 signal averaged over each colony is represented by green color intensity. Scale bar, 500 μm.

(B) Colonies colored by their oscillation phase. Scale bar, 500 μm.

(C) Plot showing oscillation phase of each colony and its distance from the center of the array. Black dots represent individual colonies. Solid line, mean; shaded area, SD. Positive slope of the line indicates waves traveling from edge to inside of the array.

(D) Bar graph of oscillations of HES7 amplitude of organoids treated with IWP-2 (2 μM, n = 3), DAPT (25 μM, n = 4), PD0325901 (1 μM, n = 5), and unperturbed control (n = 15). Amplitude of the oscillations was calculated by normalizing the amplitude of fourth peak after the treatment by the amplitude of first peak after the treatment. Bars represent the mean; whiskers represent the SD. Black dots represent individual organoids.

(E) Stills from time-lapse imaging of organoids with HES7 (green) and MESP2 (red) expression reporters for (Top: unperturbed control; bottom: FGF4 addition). Time interval between images is 15 min. Scale bar, 100 μm.

(F) Plots showing the phase profile of the organoids treated with FGF4 (left) and CHIR (right) compared to unperturbed control organoids (see STAR Methods). Lines represent mean and shaded area represents SD over (Left: FGF4, n = 9; control, n = 14, right: CHIR, n = 10; control, n = 9) biologically independent replicates.

(G) Plot showing the oscillation period profile of the organoids treated with FGF4 (red) compared to unperturbed control (blue) organoids (see STAR Methods). Lines represent mean and shaded area represents SD over (FGF4, n = 9; control, n = 14) biologically independent replicates.

(H) Top left: kymograph of NOTCH activity in control (unperturbed) PSM generated by the numerical simulation of a simple mathematical model shows anteriorly propagating HES7 waves (green) and MESP2 (red) expression (compare with Figure 3C). Bottom left: snapshots from the same simulation of the PSM, at consecutive time points, show anteriorly propagating NOTCH waves (green) and posteriorly moving somite front (red), consistent with the kymograph. Top right: numerical simulation results for the length of the somitic mesoderm in unperturbed and FGF-treated models are shown. FGF treatment slows the determination front propagation, consistent with the experiments. Bottom right: snapshot from the numerical simulations of the PSM at consecutive time points, in which FGF signaling was stimulated at 25 h. HES7 (green) and MESP2 (red). FGF treatment results in loss of segmentation clock waves, synchronous oscillations through PSM, decelerated somite determination front, and somite polarity defects.

(I) Proposed mechanism for A-P patterning of paraxial mesoderm wherein FGF gradient controls wave propagation, somite segmentation, and determination front propagation while FGF and WNT together control axial elongation.

See also Figure S6 and Videos S3 and S4.

FGF pathway results in synchronous oscillations throughout the A-P axis and a loss of traveling segmentation clock waves by accelerating the oscillations anteriorly. A simple mathematical model in which the level of FGF pathway activity determines both the oscillation frequency of the NOTCH targets and the determination front position is sufficient to produce anteriorly traveling clock waves, posteriorly moving determination fronts, and anteroposteriorly polarized somite segmentation (Figure 5H, see STAR Methods). Thus, the FGF pathway plays a central role in orchestrating the dynamics of axial patterning and morphogenesis in humans (Figure 5I).

Limitations of the study

Though we demonstrated the robustness of our approach *in vitro,* how symmetry is broken robustly *in vivo* remains an open question. One speculation is that the signals that the coupled organoids secrete to break symmetry coherently are secreted *in vivo* by the surrounding tissues with the appropriate spatial profiles. Our research exploited the robust *in vitro* system to study axial elongation and patterning. We also note that the mathematical model is for illustrative purposes only, given the lack of knowledge of most parameters for a more detailed model. We intended to show how signaling gradient-driven traveling waves and moving somite determination fronts are possible in such simple models. The experiments on humans necessarily involve *in vitro* systems. Comparisons to other mammals, in the case of conserved features, will be necessary to address the *in vivo* relevance of these results. Lastly, we have used the word "organoid" throughout this paper to describe an organized aggregate of stem cell derivatives that undergo morphogenesis. Although a term like "organized stem cell-derived aggregate" is more accurate, we use organoid as it has been routinely used as such in the literature.

STAR★METHODS

Detailed methods are provided in the online version of this paper and include the following:

- KEY RESOURCES TABLE
- RESOURCE AVAILABILITY
  - Lead contact
  - Materials availability
  - Data and code availability
- EXPERIMENTAL MODELS AND SUBJECT DETAILS
  - Cell lines
- METHOD DETAILS
  - Microfabrication and soft lithography
  - Glass micropatterning
  - Generation of human axial organoids
  - Sample fixation and immunostaining
  - Hybridization chain reaction (HCR) of organoids
  - Wide-field microscopy
  - Confocal imaging of fixed and live samples
  - Time-lapse imaging of organoids
  - Micropatterning, passivation of glass coverslips and time-lapse of micropatterned colonies
  - Single-cell RNA sequencing
  - Processing of scRNA-seq data
  - Comparison of cell types with *in vivo* mouse cells
  - Simulations
- QUANTIFICATION AND STATISTICAL ANALYSIS
  - Analysis of time-lapse imaging data and generation of kymographs
  - Quantification of phase and frequency profile on anteroposterior axis and amplitude of oscillations

SUPPLEMENTAL INFORMATION

Supplemental information can be found online at https://doi.org/10.1016/j.cell.2022.12.042.

ACKNOWLEDGMENTS

We thank Nicole Ramirez, Claire Reardon, and the Bauer Core at Harvard University for their work on the RNA sequencing used in this manuscript and for their expertise and assistance with flow cytometry and FACS. We thank the Douglas Richardson and the Harvard Center for Biological Imaging for help and advice. We thank the Weitz lab and Perry Ellis for advice and help with microfabrication. We thank members of the Ramanathan Lab and in particular, Roya Huang who built a CRISPRI line which was not eventually used in this work, Giridhar Anand, Deniz Cihat Aksel, Theresa Weis, William Weiter, and Mustafa Basaran for their help with experiments and advice. We thank Margarete Diaz-Cuadros and the Pourquie lab for sharing the HES7:Achilles/MESP2:mCherry iPSC line used for imaging. We thank Olivier Pourquie, Richard Losick, Richard Harland and Jessica Whited for advice and valuable discussions. We also thank three anonymous reviewers for their valuable comments and suggestions. This work was supported in part by NIH R01GM131105, R01MH123948 (S.R.) and by start-up funds from Harvard University.

AUTHOR CONTRIBUTIONS

Y.I.Y. and S.R. designed the study. Y.I.Y. performed the data analysis and simulations. Y.I.Y. and S.R. wrote the manuscript.

DECLARATION OF INTERESTS

Harvard University has submitted patent applications relevant to the findings reported in this study (# 63/430,298).

Received: May 10, 2022
Revised: September 29, 2022
Accepted: December 21, 2022
Published: January 18, 2023

REFERENCES

1. Gouti, M., Delile, J., Stamataki, D., Wymeersch, F.J., Huang, Y., Kleinjung, J., Wilson, V., and Briscoe, J. (2017). A gene regulatory network balances neural and mesoderm specification during vertebrate trunk development. Dev. Cell *41*, 243–261.e7. https://doi.org/10.1016/j.devcel.2017.04.002.
2. Hubaud, A., and Pourquié, O. (2014). Signalling dynamics in vertebrate segmentation. Nat. Rev. Mol. Cell Biol. *15*, 709–721. https://doi.org/10.1038/nrm3891.
3. Pourquié, O. (2011). Vertebrate segmentation: from cyclic gene networks to scoliosis. Cell *145*, 650–663. https://doi.org/10.1016/j.cell.2011.05.011.
4. Gouti, M., Metzis, V., and Briscoe, J. (2015). The route to spinal cord cell types: a tale of signals and switches. Trends Genet. *31*, 282–289. https://doi.org/10.1016/j.tig.2015.03.001.
5. Dequéant, M.L., Glynn, E., Gaudenz, K., Wahl, M., Chen, J., Mushegian, A., and Pourquié, O. (2006). A complex oscillating network of signaling

genes underlies the mouse segmentation clock. Science *314*, 1595–1598. https://doi.org/10.1126/science.1133141.

6. Palmeirim, I., Henrique, D., Ish-Horowicz, D., and Pourquié, O. (1997). Avian hairy gene expression identifies a molecular clock linked to vertebrate segmentation and somitogenesis. Cell *91*, 639–648. https://doi.org/10.1016/s0092-8674(00)80451-1.
7. Aulehla, A., Wehrle, C., Brand-Saberi, B., Kemler, R., Gossler, A., Kanzler, B., and Herrmann, B.G. (2003). Wnt3a plays a major role in the segmentation clock controlling somitogenesis. Dev. Cell *4*, 395–406. https://doi.org/10.1016/s1534-5807(03)00055-8.
8. Hayashi, S., Shimoda, T., Nakajima, M., Tsukada, Y., Sakumura, Y., Dale, J.K., Maroto, M., Kohno, K., Matsui, T., and Bessho, Y. (2009). Sprouty4, an FGF inhibitor, displays cyclic gene expression under the control of the notch segmentation clock in the mouse PSM. PLoS One *4*, e5603. https://doi.org/10.1371/journal.pone.0005603.
9. Dubrulle, J., and Pourquié, O. (2004). fgf8 mRNA decay establishes a gradient that couples axial elongation to patterning in the vertebrate embryo. Nature *427*, 419–422. https://doi.org/10.1038/nature02216.
10. Amin, S., Neijts, R., Simmini, S., van Rooijen, C., Tan, S.C., Kester, L., van Oudenaarden, A., Creyghton, M.P., and Deschamps, J. (2016). Cdx and T brachyury co-activate growth signaling in the embryonic axial progenitor niche. Cell Rep. *17*, 3165–3177. https://doi.org/10.1016/j.celrep.2016.11.069.
11. Bénazéraf, B., Francois, P., Baker, R.E., Denans, N., Little, C.D., and Pourquié, O. (2010). A random cell motility gradient downstream of FGF controls elongation of an amniote embryo. Nature *466*, 248–252. https://doi.org/10.1038/nature09151.
12. Wymeersch, F.J., Wilson, V., and Tsakiridis, A. (2021). Understanding axial progenitor biology in vivo and in vitro. Development *148*, dev180612. https://doi.org/10.1242/dev.180612.
13. Dubrulle, J., McGrew, M.J., and Pourquié, O. (2001). FGF signaling controls somite boundary position and regulates segmentation clock control of spatiotemporal Hox gene activation. Cell *106*, 219–232. https://doi.org/10.1016/s0092-8674(01)00437-8.
14. Aulehla, A., Wiegraebe, W., Baubet, V., Wahl, M.B., Deng, C., Taketo, M., Lewandoski, M., and Pourquié, O. (2008). A beta-catenin gradient links the clock and wavefront systems in mouse embryo segmentation. Nat. Cell Biol. *10*, 186–193. https://doi.org/10.1038/ncb1679.
15. Naiche, L.A., Holder, N., and Lewandoski, M. (2011). FGF4 and FGF8 comprise the wavefront activity that controls somitogenesis. Proc. Natl. Acad. Sci. USA *108*, 4018–4023. https://doi.org/10.1073/pnas.1007417108.
16. Dunty, W.C., Jr., Biris, K.K., Chalamalasetty, R.B., Taketo, M.M., Lewandoski, M., and Yamaguchi, T.P. (2008). Wnt3a/beta-catenin signaling controls posterior body development by coordinating mesoderm formation and segmentation. Development *135*, 85–94. https://doi.org/10.1242/dev.009266.
17. Diaz-Cuadros, M., and Pourquie, O. (2021). In vitro systems: a new window to the segmentation clock. Dev. Growth Differ. *63*, 140–153. https://doi.org/10.1111/dgd.12710.
18. Diaz-Cuadros, M., Wagner, D.E., Budjan, C., Hubaud, A., Tarazona, O.A., Donelly, S., Michaut, A., Al Tanoury, Z., Yoshioka-Kobayashi, K., Niino, Y., et al. (2020). In vitro characterization of the human segmentation clock. Nature *580*, 113–118. https://doi.org/10.1038/s41586-019-1885-9.
19. Matsuda, M., Yamanaka, Y., Uemura, M., Osawa, M., Saito, M.K., Nagahashi, A., Nishio, M., Guo, L., Ikegawa, S., Sakurai, S., et al. (2020). Recapitulating the human segmentation clock with pluripotent stem cells. Nature *580*, 124–129. https://doi.org/10.1038/s41586-020-2144-9.
20. Chu, L.F., Mamott, D., Ni, Z., Bacher, R., Liu, C., Swanson, S., Kendziorski, C., Stewart, R., and Thomson, J.A. (2019). An in vitro human segmentation clock model derived from embryonic stem cells. Cell Rep. *28*, 2247–2255.e5. https://doi.org/10.1016/j.celrep.2019.07.090.
21. Veenvliet, J.V., Bolondi, A., Kretzmer, H., Haut, L., Scholze-Wittler, M., Schifferl, D., Koch, F., Guignard, L., Kumar, A.S., Pustet, M., et al. (2020). Mouse embryonic stem cells self-organize into trunk-like structures with neural tube and somites. Science *370*, eaba4937. https://doi.org/10.1126/science.aba4937.
22. van den Brink, S.C., Alemany, A., van Batenburg, V., Moris, N., Blotenburg, M., Vivié, J., Baillie-Johnson, P., Nichols, J., Sonnen, K.F., Martinez Arias, A., and van Oudenaarden, A. (2020). Single-cell and spatial transcriptomics reveal somitogenesis in gastruloids. Nature *582*, 405–409. https://doi.org/10.1038/s41586-020-2024-3.
23. Sanaki-Matsumiya, M., Matsuda, M., Gritti, N., Nakaki, F., Sharpe, J., Trivedi, V., and Ebisuya, M. (2022). Periodic formation of epithelial somites from human pluripotent stem cells. Nat. Commun. *13*, 2325. https://doi.org/10.1038/s41467-022-29967-1.
24. Gupta, A., Lutolf, M.P., Hughes, A.J., and Sonnen, K.F. (2021). Bioengineering in vitro models of embryonic development. Stem Cell Rep. *16*, 1104–1116. https://doi.org/10.1016/j.stemcr.2021.04.005.
25. Anand, G.M., Megale, H.C., Murphy, S.H., Weis, T., Lin, Z., He, Y., Wang, X., Liu, J., and Ramanathan, S. (2023). Controlling organoid symmetry breaking uncovers an excitable system underlying human axial elongation. Cell *186*. https://doi.org/10.1016/j.cell.2022.12.043.
26. Zheng, Y., Xue, X., Shao, Y., Wang, S., Esfahani, S.N., Li, Z., Muncie, J.M., Lakins, J.N., Weaver, V.M., Gumucio, D.L., and Fu, J. (2019). Controlled modelling of human epiblast and amnion development using stem cells. Nature *573*, 421–425. https://doi.org/10.1038/s41586-019-1535-2.
27. Oginuma, M., Niwa, Y., Chapman, D.L., and Saga, Y. (2008). Mesp2 and Tbx6 cooperatively create periodic patterns coupled with the clock machinery during mouse somitogenesis. Development *135*, 2555–2562. https://doi.org/10.1242/dev.019877.
28. Saga, Y., Hata, N., Koseki, H., and Taketo, M.M. (1997). Mesp2: a novel mouse gene expressed in the presegmented mesoderm and essential for segmentation initiation. Genes Dev. *11*, 1827–1839. https://doi.org/10.1101/gad.11.14.1827.
29. Takahashi, Y., Koizumi, K., Takagi, A., Kitajima, S., Inoue, T., Koseki, H., and Saga, Y. (2000). Mesp2 initiates somite segmentation through the Notch signalling pathway. Nat. Genet. *25*, 390–396. https://doi.org/10.1038/78062.
30. Friedman, J., Hastie, T., and Tibshirani, R. (2001). The Elements of Statistical Learning (Springer series in statistics New York).
31. Melton, S., and Ramanathan, S. (2021). Discovering a sparse set of pairwise discriminating features in high-dimensional data. Bioinformatics *37*, 202–212. https://doi.org/10.1093/bioinformatics/btaa690.
32. Cooper, F., Gentsch, G.E., Mitter, R., Bouissou, C., Healy, L.E., Rodriguez, A.H., Smith, J.C., and Bernardo, A.S. (2022). Rostrocaudal patterning and neural crest differentiation of human pre-neural spinal cord progenitors in vitro. Stem Cell Rep. *17*, 894–910. https://doi.org/10.1016/j.stemcr.2022.02.018.
33. Williams, B.A., and Ordahl, C.P. (1994). Pax-3 expression in segmental mesoderm marks early stages in myogenic cell specification. Development *120*, 785–796. https://doi.org/10.1242/dev.120.4.785.
34. Beckers, A., Alten, L., Viebahn, C., Andre, P., and Gossler, A. (2007). The mouse homeobox gene Noto regulates node morphogenesis, notochordal ciliogenesis, and left right patterning. Proc. Natl. Acad. Sci. USA *104*, 15765–15770. https://doi.org/10.1073/pnas.0704344104.
35. Resende, T.P., Ferreira, M., Teillet, M.A., Tavares, A.T., Andrade, R.P., and Palmeirim, I. (2010). Sonic hedgehog in temporal control of somite formation. Proc. Natl. Acad. Sci. USA *107*, 12907–12912. https://doi.org/10.1073/pnas.1000979107.
36. Haghverdi, L., Büttner, M., Wolf, F.A., Buettner, F., and Theis, F.J. (2016). Diffusion pseudotime robustly reconstructs lineage branching. Nat. Methods *13*, 845–848. https://doi.org/10.1038/nmeth.3971.
37. Grifone, R., Demignon, J., Houbron, C., Souil, E., Niro, C., Seller, M.J., Hamard, G., and Maire, P. (2005). Six1 and Six4 homeoproteins are required for Pax3 and Mrf expression during myogenesis in the mouse embryo. Development *132*, 2235–2249. https://doi.org/10.1242/dev.01773.

38. Aulehla, A., and Pourquié, O. (2010). Signaling gradients during paraxial mesoderm development. Cold Spring Harb. Perspect. Biol. *2*, a000869. https://doi.org/10.1101/cshperspect.a000869.

39. Diez del Corral, R., Olivera-Martinez, I., Goriely, A., Gale, E., Maden, M., and Storey, K. (2003). Opposing FGF and retinoid pathways control ventral neural pattern, neuronal differentiation, and segmentation during body axis extension. Neuron *40*, 65–79. https://doi.org/10.1016/s0896-6273(03)00565-8.

40. Sasai, N., Kutejova, E., and Briscoe, J. (2014). Integration of signals along orthogonal axes of the vertebrate neural tube controls progenitor competence and increases cell diversity. PLoS Biol. *12*, e1001907. https://doi.org/10.1371/journal.pbio.1001907.

41. Conlon, R.A., Reaume, A.G., and Rossant, J. (1995). Notch1 is required for the coordinate segmentation of somites. Development *121*, 1533–1545.

42. Moore, R., and Alexandre, P. (2020). Delta-notch signaling: the long and the short of a neuron's influence on progenitor fates. J. Dev. Biol. *8*, 8. https://doi.org/10.3390/jdb8020008.

43. Wilson, L., and Maden, M. (2005). The mechanisms of dorsoventral patterning in the vertebrate neural tube. Dev. Biol. *282*, 1–13. https://doi.org/10.1016/j.ydbio.2005.02.027.

44. Sagner, A., and Briscoe, J. (2019). Establishing neuronal diversity in the spinal cord: a time and a place. Development *146*, dev182154. https://doi.org/10.1242/dev.182154.

45. Ebensperger, C., Wilting, J., Brand-Saberi, B., Mizutani, Y., Christ, B., Balling, R., and Koseki, H. (1995). Pax-1, a regulator of sclerotome development is induced by notochord and floor plate signals in avian embryos. Anat. Embryol. *191*, 297–310. https://doi.org/10.1007/BF00534682.

46. Falk, H.J., Tomita, T., Monke, G., McDole, K., and Aulehla, A. (2022). Imaging the onset of oscillatory signaling dynamics during mouse embryo gastrulation. Development *149*, dev200083. https://doi.org/10.1242/dev.200083.

47. Ferjentsik, Z., Hayashi, S., Dale, J.K., Bessho, Y., Herreman, A., De Strooper, B., del Monte, G., de la Pompa, J.L., and Maroto, M. (2009). Notch is a critical component of the mouse somitogenesis oscillator and is essential for the formation of the somites. PLoS Genet. *5*, e1000662. https://doi.org/10.1371/journal.pgen.1000662.

48. Niwa, Y., Shimojo, H., Isomura, A., González, A., Miyachi, H., and Kageyama, R. (2011). Different types of oscillations in Notch and Fgf signaling regulate the spatiotemporal periodicity of somitogenesis. Genes Dev. *25*, 1115–1120. https://doi.org/10.1101/gad.2035311.

49. Ishimatsu, K., Hiscock, T.W., Collins, Z.M., Sari, D.W.K., Lischer, K., Richmond, D.L., Bessho, Y., Matsui, T., and Megason, S.G. (2018). Size-reduced embryos reveal a gradient scaling-based mechanism for zebrafish somite formation. Development *145*, dev161257. https://doi.org/10.1242/dev.161257.

50. Simsek, M.F., and Özbudak, E.M. (2018). Spatial fold change of FGF signaling encodes positional information for segmental determination in zebrafish. Cell Rep. *24*, 66–78.e8. https://doi.org/10.1016/j.celrep.2018.06.023.

51. Sawada, A., Shinya, M., Jiang, Y.J., Kawakami, A., Kuroiwa, A., and Takeda, H. (2001). Fgf/MAPK signalling is a crucial positional cue in somite boundary formation. Development *128*, 4873–4880.

52. Oginuma, M., Moncuquet, P., Xiong, F., Karoly, E., Chal, J., Guevorkian, K., and Pourquié, O. (2017). A gradient of glycolytic activity coordinates FGF and Wnt signaling during elongation of the body axis in amniote embryos. Dev. Cell *40*, 342–353.e10. https://doi.org/10.1016/j.devcel.2017.02.001.

53. Regev, I., Guevorkian, K., Gupta, A., Pourquie, O., and Mahadevan, L. (2022). Rectified random cell motility as a mechanism for embryo elongation. Development *149*, dev199423. https://doi.org/10.1242/dev.199423.

54. Michaut, A., Mongera, A., Gupta, A., Serra, M., Rigoni, P., Lee, J.G., Duarte, F., Hall, A.R., Mahadevan, L., Guevorkian, K., and Pourquié, O. (2022). Activity-driven extracellular volume expansion drives vertebrate axis elongation. Preprint at bioRxiv. https://doi.org/10.1101/2022.06.27.497799.

55. Schindelin, J., Arganda-Carreras, I., Frise, E., Kaynig, V., Longair, M., Pietzsch, T., Preibisch, S., Rueden, C., Saalfeld, S., Schmid, B., et al. (2012). Fiji: an open-source platform for biological-image analysis. Nat. Methods *9*, 676–682. https://doi.org/10.1038/nmeth.2019.

56. Berg, S., Kutra, D., Kroeger, T., Straehle, C.N., Kausler, B.X., Haubold, C., Schiegg, M., Ales, J., Beier, T., Rudy, M., et al. (2019). ilastik: interactive machine learning for (bio)image analysis. Nat. Methods *16*, 1226–1232. https://doi.org/10.1038/s41592-019-0582-9.

57. Gritti, N., Lim, J.L., Anlas, K., Pandya, M., Aalderink, G., Martinez-Ara, G., and Trivedi, V. (2021). MOrgAna: accessible quantitative analysis of organoids with machine learning. Development *148*, dev199611. https://doi.org/10.1242/dev.199611.

58. Wolf, F.A., Angerer, P., and Theis, F.J. (2018). SCANPY: large-scale single-cell gene expression data analysis. Genome Biol. *19*, 15. https://doi.org/10.1186/s13059-017-1382-0.

59. Vianello, S.D., Park, J., and Lutolf, M. (2021). Hybridization chain reaction (HCR) protocol for Gastruloids (ESC aggregates). protocols.io. https://doi.org/10.17504/protocols.io.bcwfixbn.

60. Wymeersch, F.J., Skylaki, S., Huang, Y., Watson, J.A., Economou, C., Marek-Johnston, C., Tomlinson, S.R., and Wilson, V. (2019). Transcriptionally dynamic progenitor populations organised around a stable niche drive axial patterning. Development *146*, dev168161. https://doi.org/10.1242/dev.168161.

61. Goldbeter, A., Gonze, D., and Pourquié, O. (2007). Sharp developmental thresholds defined through bistability by antagonistic gradients of retinoic acid and FGF signaling. Dev. Dyn. *236*, 1495–1508. https://doi.org/10.1002/dvdy.21193.

62. Jaeger, J., and Goodwin, B.C. (2001). A cellular oscillator model for periodic pattern formation. J. Theor. Biol. *213*, 171–181. https://doi.org/10.1006/jtbi.2001.2414.

63. Oginuma, M., Takahashi, Y., Kitajima, S., Kiso, M., Kanno, J., Kimura, A., and Saga, Y. (2010). The oscillation of Notch activation, but not its boundary, is required for somite border formation and rostral-caudal patterning within a somite. Development *137*, 1515–1522. https://doi.org/10.1242/dev.044545.

64. Delaune, E.A., François, P., Shih, N.P., and Amacher, S.L. (2012). Single-cell-resolution imaging of the impact of Notch signaling and mitosis on segmentation clock dynamics. Dev. Cell *23*, 995–1005. https://doi.org/10.1016/j.devcel.2012.09.009.

Please cite this article in press as: Yaman and Ramanathan, Controlling human organoid symmetry breaking reveals signaling gradients drive segmentation clock waves, Cell (2023), https://doi.org/10.1016/j.cell.2022.12.042

STAR★METHODS

KEY RESOURCES TABLE

REAGENT or RESOURCE	SOURCE	IDENTIFIER
Antibodies		
Rat Monoclonal Anti-SOX2	Thermo Fisher Scientific	RRID:AB_11219471
Mouse Monoclonal Anti-ZO1	Thermo Fisher Scientific	RRID:AB_2532187
Goat Polyclonal Anti-SOX1	R and D Systems	RRID:AB_2239879
Goat Polyclonal Anti-Brachyury	R and D Systems	RRID:AB_2200235
Goat Polyclonal Anti-TBX6	R and D Systems	RRID:AB_2200834
Mouse Monoclonal Anti-PAX6	BD Biosciences	RRID:AB_10715442
Mouse Monoclonal Anti-β-Catenin	BD Biosciences	RRID:AB_397554
Rabbit Monoclonal Anti-N-Cadherin	Cell Signaling Technology	RRID:AB_2687616
Rabbit Polyclonal Pan p44/42 MAPK (phosphorylated Erk1/2)	Cell Signaling Technology	RRID:AB_331646
Chemicals, peptides, and recombinant proteins		
mTeSR™ Plus	StemCell Technologies	5825
ReLeSR	StemCell Technologies	5872
TeSR™-E6	StemCell Technologies	05,946
Matrigel hESC-qualified Matrix, *LDEV-Free	Corning	354277
Heparin sodium salt from porcine intestinal mucosa	Millipore	H3393-100KU
CHIR-99021	Selleck Chemicals	S2924
PD0325901	Selleck Chemicals	S1036
N-2 Supplement	Thermo Fisher Scientific	17502048
B-27™ Supplement (50X), minus vitamin A	Thermo Fisher Scientific	12587010
LDN 193189 dihydrochloride	R and D Systems	6053/10
Penicillin-Streptomycin	Millipore	P4458
rhFGF4	R and D Systems	235-F4-025
DMEM/F-12, HEPES, no phenol red	Thermo Fisher Scientific	11039021
GlutaMAX™ Supplement	Thermo Fisher Scientific	35050061
Insulin-Transferrin-Selenium (ITS -G) (100X)	Thermo Fisher Scientific	41400045
MEM Non-Essential Amino Acids Solution (100X)	Thermo Fisher Scientific	11140050
2-Mercaptoethanol	Thermo Fisher Scientific	21985023
BSA solution	Millipore	A9576
Deposited data		
Single cell RNA-seq data	This study	NCBI GEO: GSE220563
Single cell RNA-seq data	Diaz-Cuadros et al.[18]	NCBI GEO: GSE114186
Experimental models: Cell lines		
HES7-Achilles; MESP2-mCherry iPSC line	Laboratory of Olivier Pourquié	N/A
Software and algorithms		
Zen	Zeiss	https://www.zeiss.com/microscopy/en/products/software/zeiss-zen.html
Fiji/ImageJ	Schindelin et al.[55]	https://imagej.net/software/fiji/
Arivis Vision4D	Arivis	https://www.arivis.com/
ilastik	Berg et al.[56]	https://www.ilastik.org/index.html
MATLAB	MathWorks	https://www.mathworks.com/products/matlab.html

(*Continued on next page*)

Please cite this article in press as: Yaman and Ramanathan, Controlling human organoid symmetry breaking reveals signaling gradients drive segmentation clock waves, Cell (2023), https://doi.org/10.1016/j.cell.2022.12.042

Continued

REAGENT or RESOURCE	SOURCE	IDENTIFIER
MOrgAna	Gritti et al.[57]	https://github.com/LabTrivedi/MOrgAna
Scanpy	Wolf et al.[58]	https://scanpy.readthedocs.io/en/stable/
Scripts used for analyzing kymographs, scRNA-seq and script for mathematical model	This paper	https://doi.org/10.5281/zenodo.7458178

RESOURCE AVAILABILITY

Lead contact

Further information and requests for resources and reagents should be directed to and will be fulfilled by the lead contact, Sharad Ramanathan (sharad@cgr.harvard.edu).

Materials availability

This study did not generate new unique reagents.

Data and code availability

- Single-cell RNA-seq data have been deposited at GEO and are publicly available as of the date of publication. Accession numbers are listed in the key resources table. Microscopy data reported in this paper will be shared by the lead contact upon request.
- All original code has been deposited at Zenodo and is publicly available as of the date of publication. DOIs are listed in the key resources table.
- Any additional information required to reanalyze the data reported in this paper is available from the lead contact upon request.

EXPERIMENTAL MODELS AND SUBJECT DETAILS

Cell lines

All experiments were conducted using NCRM1 iPS cells with endogenous locus of HES7 tagged with Achilles and MESP2 tagged with mCherry (provided generously by the Pourquie Lab). Sex is not a relevant parameter for this study. iPSCs were cultured in 6-well tissue culture dishes treated for 1 h with 1X diluted Matrigel (Corning) and supplied with mTeSR Plus media (STEMCELL Technologies). Media is changed with fresh media every two days. For routine culture, we passaged by washing with Dulbecco's PBS (DPBS) followed by ReLeSR (STEMCELL Technologies) treatment. Briefly, cells after washing with DPBS, cells are treated with ReLeSR for 30 s. Then ReLeSR is aspirated and cells are incubated in the incubation chamber (37°C, 5%CO_2) for 5 min. Cells are rescued using 1 mL of mTeSR Plus. 25 μL of the cell suspension is added to a well of a 6-well plate coated with Matrigel. All cell lines used were routinely tested for mycoplasma contamination (Mycoplasma PCR Detection Kit, ABM Cat. No. G238). We used hiPSCs in accordance with approvals by Harvard University IRB (protocol #IRB18- 0665) and Harvard University ESCRO (protocol E00065).

METHOD DETAILS

Microfabrication and soft lithography

Briefly, round ADEX-50 dry film photoresist films (DJ Microlaminates) were laminated onto round 76.2 mm Si wafers (University Wafers) at 65°C using an SKY laminator. Films were exposed through 8 μm-resolution photomasks (CAD/Art Services) to 365 nm UV light at an intensity of 25 mW/cm^2 for 13 s using a UV lamp (Uvitron), baked at 80°C for 15 min, and developed face down in cyclohexanone on a steel mesh without shaking for 5 min, followed by washing with acetone and isopropyl alcohol and drying with compressed air. Afterward, masters were hard-baked on a hot plate at 200°C for 1 h and silanized for 1 h in a vacuum chamber with 50 μL of trichloro(1H,1H,2H,2H-perfluorooctyl) silane. To cast PDMS, the elastomer base and curing agent (Dow SYLGARD™ 184, Ellsworth Adhesives) were mixed at a ratio of 1:9, degassed, poured onto masters, and baked at 80°C for 1 h. Stamps were covered with Scotch tape to prevent dust accumulation and cut using a scalpel.

Glass micropatterning

PDMS stamps were treated with 1X Matrigel overnight at room temperature. Stamps were washed with MilliQ water and dried using pressurized air. Stamps were brought into contact on the features-side to the glass coverslips (22 mm No. 1.5 square borosilicate glass coverslips (VWR)) and gently pressed with a tweezer to ensure contact. Stamps were removed after 30–60 s, and coverslips were submerged into PBS for storage at 4°C until cell seeding.

Generation of human axial organoids

hPSC colonies on maintenance plate were washed with DPBS twice and incubated in Accutase for 10 min in 37°C incubators. Cells were resuspended as single cells at 1.5 M/mL density in mTeSR + containing 10 mM Y27632. Micropatterned coverslips were mounted in 6-well glass bottom plates using silicone grease. 2 mL of the suspension was pipetted onto micropatterned coverslips and incubated at 37°C incubator for 75 min. Excess media and non-adherent cells were removed by aspiration, coverslips were washed twice with pre-warmed DPBS and replaced with mTeSR + containing 10 mM Y27632. Cells were incubated overnight. On the following day, the media was replaced with mTeSR+ and cells were incubated overnight again. After 48 h from initial seeding, cells formed confluent colonies on micropatterns.

The differentiation was started by adding N2B27(DMEM/F12 with 1X N2, 1X B27 minus vitamin A, 1X penicillin/streptomycin, 1% NEAA, 0.5% GlutaMAX, 0.1% β-mercaptoethanol, and 0.05% BSA) media containing Matrigel (6%, v/v) supplemented with 4 μM CHIR99021 (CHIR), 0.5 μM LDN193189 (LDN) and 5 μM A83-01. The time of initiation of differentiation was denoted as timepoint 0. At 48 h, organoids with a single lumen on micropatterns could be observed. At this point, the media was replaced with E6, and organoids were removed from the surface using a cell scraper. Each organoid as moved to a well of a 96-well Low Bind plate containing 100 μL E6 and incubated overnight. At 72 h, E6 containing Matrigel was added to the wells, making the final Matrigel concentration 6% v/v. Organoids were incubated in this media for the following 48 h. For extended incubation, additional 100 μL E6 was added to the wells.

Sample fixation and immunostaining

Organoids were collected from 96-well plates and washed twice in DPBS before fixation in 4% PFA for 20 min at room temperature. After the fixation, organoids were washed three times in PBS, then stored at 4°C until the blocking step. Organoids were permeabilized and blocked in PBS with 0.3% Triton X-100 and 5% Normal Donkey Serum for 60 min at room temperature. Primary antibodies were diluted in antibody dilution buffer (1X PBS, 1% BSA, 0.3% Triton X-100) and incubated overnight at 4°C with gentle rocking. After the primary staining step, organoids were washed three times in PBS for 5 min and incubated in Alexa-Fluor-conjugated secondary antibodies and DAPI diluted in antibody dilution buffer overnight at 4°C with gentle rocking. Finally, organoids were washed three times in PBS and imaged. The following primary antibodies were used at the indicated dilutions: Rat anti-SOX2 (1:400, Thermo Fisher BTJCE), Rabbit anti-NCadherin (1:400, Cell Signaling D4R1H), Mouse anti-ZO1-FITC (1:800, Thermo Fisher 1A12), Goat anti-SOX1 (1:400, R&D AF3369), Goat anti-TBXT (1:400, R&D AF2085), Goat anti-TBX6 (1:400, R&D AF4744), Mouse anti-PAX6(1:400, BD Biosciences 561,462), Mouse anti-β-catenin (1:400, BD Biosciences 610,153), Rabbit anti-dpERK(1:200, Cell Signaling 9101). In the immunostainings for dpERK and β-catenin, the first two wash steps were skipped, and organoids were fixed in 96-well V-bottom plate by adding certain amount of 10% PFA to the media to have organoids in 4% PFA final concentration. In the case of dpERK staining, organoids were dehydrated in cold methanol for 10 min at −20°C followed by three PBS washes. The rest of the standard protocol were followed for dpERK and β-catenin immunostainings.

Hybridization chain reaction (HCR) of organoids

HCR was performed on organoids following the previously published protocol.[59] Briefly, organoids were fixed in 2% formaldehyde overnight. The next day, organoids were washed 2 times with PBST (0.1% Tween 20 in 1xPBS) for 5 min and dehydrated with a series of graded methanol washes with 25%, 50%, 75%, and two times 100% methanol in PBST, 5 min for each wash. Samples were incubated overnight or until use at −20°C. The next day, samples were rehydrated through a series of graded methanol washes with 100%, 75%, 50%, and 25% methanol in PBST and two times with 100% PBST for 5 min each. Samples were treated with 25 μg/mL proteinase K for 4 min at room temperature and washed twice with PBST for 5 min each. Samples were refixed in 4% formaldehyde for 20 min at room temperature, then washed 3 times with PBST. Later, samples were washed with pre-warmed PH buffer at 37°C for 5 min. After the wash, samples were resuspended in PH buffer and incubated for 30 min at 37°C. Samples were incubated in 500 μL of PH buffer along with 4 pmol of the probe mixture overnight. On the next day, hairpin mixtures were prepared by bringing h1 and h2 of each hairpin to 95°C for 90 s and leaving it at room temperature for 30 min. Two hairpin mixtures are then added to the amplification buffer with a final concentration of 48 pM. Samples were washed with probe wash buffer at 37°C for four times, 15 min for each wash. Samples were then washed with 5xSSCT two times at room temperature, 5 min for each wash. Samples were washed once with amplification buffer for 5 min and resuspended in the hairpin mixture, incubated overnight at room temperature. On the final day, organoids were washed with 5x SSCT for 30 min at room temperature and nuclei were stained with washing organoids in the 1:1000 DAPI (2 μg/mL) three times, 25 min for each wash. Finally, samples were washed two times for 15 min with 5xSSCT at room temperature and imaged. HCR probe design was: FGF4 (Accession NM_002007), FGF8 (Accession NM_033163), WNT3A (Accession NM_033131), CYP26A1 (Accession NM_057157), ALDH1A2 (Accession NM_170697).

Wide-field microscopy

Axial organoids at 72h, 96h and 120h stage were imaged using a Zeiss AxioObserver Z1 inverted microscope in a humidified incubator (5% CO2, 37°C), with a Zeiss EC Plan-Neofluar 10x/0.30 NA objective. The 43 HE dsRed/46 HE YFP/47 HE CFP/49 DAPI/50 Cy5 filter sets from Zeiss were used. Images were acquired using an Orca-Flash 4.0 CMOS camera (Hamamatsu). The microscope was controlled using ZEN software. All images were analyzed using Fiji,[55] Ilastik,[56] MATLAB, Morgana[57] or Python.

Confocal imaging of fixed and live samples

Fixed samples were imaged on a Zeiss LSM 980 with Airyscan using a Zeiss 10x (NA 0.45) objective. Detection was performed on DAPI, Alexa Fluor 488, Alexa Fluor 568 and Alexa Fluor 647 channels. A z stack with 1-micron intervals was acquired from the lower to upper apical surface of each organoid. After Airyscan processing, a maximum Z intensity projection was performed for visualization purposes. Nuclear segmentation is done and analyzed by using Arivis Vision4D.

Time-lapse imaging of organoids

For time-lapse imaging of organoids, the method described in generation of human axial organoids was followed until 70 h of differentiation. Later, organoids were collected in a 5 mL Eppendorf tube and centrifuged at 200 rcf for 1 min. Supernatant was removed and organoids were suspended in 2 mL of basal media DGIP (DMEM F-12 no phenol red, Glutamax, Insulin-Transferrin-Selenium, Penicillin-Streptomycin). Organoids were then transferred to 96-well glass bottom plates along with 10 μL of DGIP for each organoid, each well containing 50 μL of DGIP. Following the transfer of the organoids, 50 μL of ice-cold DGIP containing 12% v/v Matrigel was added to each well, resulting 6% v/v final Matrigel concentration. The plate was then placed in humidified incubator for 2 h, allowing the Matrigel to solidify. Later, the plate was moved to Zeiss AxioObserver Z1 inverted microscope in a humidified incubator (5% CO2, 37°C) and imaging was started immediately. Imaging was done using a Zeiss EC Plan-Neofluar 10x/0.30 NA objective. Images were taken every 15 min. The 43 HE dsRed/46 HE YFP filter sets from Zeiss were used. Images were acquired using an Orca-Flash 4.0 CMOS camera (Hamamatsu) with 4x4 binning. For perturbations, time lapse was paused and 20 μL of DGIP containing the respective small molecules or recombinant proteins without removing the culturing plate from the stage. In all perturbations with FGF4 ligand, the media is supplemented with 1 μg/mL heparin (Sigma Aldrich cat. no. H3393-100KU) The microscope was controlled using ZEN software.

Micropatterning, passivation of glass coverslips and time-lapse of micropatterned colonies

PDMS stamps were treated with 1X Matrigel overnight at room temperature. Stamps were washed with MilliQ water and dried using pressurized air. Stamps were brought into contact on the features-side to the plasma treated glass coverslips (22 mm No. 1.5 square borosilicate glass coverslips (VWR)) and gently pressed with a tweezer to ensure contact. 0.1 mg/mL PLL-g-PEG buffered with 10 mM HEPES was flown between the stamp and the coverslip surface and incubated for 30 min before removing the stamp. The coverslips were washed three times with PBS and the stamp was removed. hPSC colonies on maintenance plate were washed with DPBS twice and incubated in Accutase for 10 min in 37°C incubators. Cells were resuspended as single cells at 1.5 M/mL density in mTeSR + containing 10 mM Y27632. Micropatterned coverslips were mounted in 6-well glass bottom plates using silicone grease. 2 mL of the suspension was pipetted onto micropatterned coverslips and incubated at 37°C incubator for 75 min. Excess media and non-adherent cells were removed by aspiration, coverslips were washed twice with pre-warmed DPBS and replaced with mTeSR + containing 10 mM Y27632. Cells were incubated overnight. On the following day, the media was replaced with mTeSR+ and cells were incubated overnight again. After 48 h from initial seeding, cells formed confluent colonies on micropatterns. The differentiation was started by adding N2B27(DMEM/F12 with 1X N2, 1X B27, 1X penicillin/streptomycin, 1% NEAA, 0.5% GlutaMAX, 0.1% β-mercaptoethanol, and 0.05% BSA) media containing Matrigel (6%, v/v) supplemented with 4 mM CHIR99021 (CHIR), 0.5 mM LDN193189 (LDN). The time of initiation of differentiation was denoted as timepoint 0. At 48 h of differentiation, the plate was moved to Zeiss AxioObserver Z1 inverted microscope in a humidified incubator (5% CO2, 37°C) and imaging was started immediately. In the case of FGF4 perturbation, FGF4 was added to the media right before the imaging started. Imaging was done using a Zeiss EC Plan-Neofluar 20x/0.50 NA objective. Images were taken every 15 min. The 46 HE YFP filter sets from Zeiss were used. Images were acquired using an Orca-Flash 4.0 CMOS camera (Hamamatsu) with 4x4 binning.

Single-cell RNA sequencing

Organoids were dissociated into a single-cell suspension using the Worthington Papain Dissociation System kit (Worthington Biochemical). Cells were counted on the LUNA-FX7 Automated Cell Counter (Logos Biosystems) using fluorescence detection for viability with an acridine orange/propidium iodide stain (Part No. F23011). After counting, the sample was loaded into Chip G per the user guide from 10x Genomics, and no alterations were made at any step of the protocol (Part No. CG000315). GEMs were formed targeting 10,000 cells and reverse transcription completed immediately after. The cDNA was cleaned from the GEM reagents, amplified for a total of 11 cycles and verified via TapeStation (Agilent Technologies). Amplified cDNA was diluted and ran on the 4200 TapeStation instrument using High Sensitivity D5000 tape and reagents (Part No. 5067–5592 & 5067–5593). The amplified cDNA was fragmented, end repaired, and A-tailed followed by adaptor ligation, and PCR amplification for a total of 11 cycles with each sample receiving a unique set of dual indices (Part No. 1000215). Final libraries were diluted and ran using the High Sensitivity D5000 tape and reagents (Part No. 5067–5592 & 5067–5593) on the 4200 TapeStation (Agilent Technologies). Libraries were quantified via Kapa qPCR using the Complete Universal Kit (Part No. 07960140001, Roche Sequencing Solutions) and the CFX96 Touch Real-Time PCR Detection System (Bio-Rad Laboratories). Libraries were sequenced on an Illumina NovaSeq instrument using the parameters outlined in the user guide (Read1: 28 bp, i7 index: 10 bp, i5 index: 10 bp, Read2: 90 bp). After sequencing and demultiplexing, the Cell Ranger count pipeline to align reads to the GRCh38 human reference genome and produce the associated cell by gene count matrix.

Please cite this article in press as: Yaman and Ramanathan, Controlling human organoid symmetry breaking reveals signaling gradients drive segmentation clock waves, Cell (2023), https://doi.org/10.1016/j.cell.2022.12.042

Processing of scRNA-seq data

Cells with 6,000 to 30,000 reads were subsampled to a obtain a read count of 6,000 for each cell. Sparse multimodal decomposition (SMD)[18] was performed in Python on the subsampled count matrix. Top 150 genes with a highest *Z* score from SMD were filtered to remove genes with a log normalized expression mean or SD less than 0.05, genes expressed in more than 90% or less than 1% of cells, and genes associated with the cell cycle, resulting in a list of 48 genes. In the subspace of these 48 genes, cells were hierarchically clustered, and 6 clusters were identified. Clusters were annotated manually based on differentially expressed genes. UMAP plots were generated using ScanPy.[58]

Diffusion map analysis was performed using the DPT method[19] in scanpy in the subspace of 48 genes. The root cell was selected to be a cell from the NMP cluster with the highest value along the first principal component from principal component analysis. To generate a pseudo-spatial gene expression heatmap, cells were ordered by pseudo-spatial index and their *Z* score normalized gene expression values were smoothed using a Gaussian filter with a kernel size of 50 for mesodermal clusters and 150 for neural clusters. Top 200 differentially expressed genes were selected for mesodermal and neural clusters, based on the difference of the highest and the lowest values of *Z* score normalized gene expression on respective clusters. Genes were then ordered by the pseudo-spatial position of their peaks of smoothed gene expression values.

To generate pseudo-spatial gene expression plots for individual genes, a moving average filter was applied to log-normalized gene expression values on the pseudo-spatial axis was applied to mesodermal and neural branches with an averaging width of 201 cells for mesodermal clusters and 601 for neural clusters. Later, each gene expression was normalized based on the highest expression of the gene on the respective lineage.

Comparison of cell types with *in vivo* mouse cells

To pre-process the mouse dataset, we selected cells belonging to neural and paraxial mesodermal lineages in the mouse dataset. From this subset of cells, we removed doublets and cells with low read counts by selecting cells that had between 8000 and 12,000 reads. We then normalized the read counts from each cell both in the mouse and human datasets. After log normalizing each dataset, we combined them (before which we found the corresponding homologous genes between mouse and human to map the mouse genes onto human genes). The resulting dataset consisted of 2376 mouse cells and 9096 human cells with reads from 7989 genes. From these genes we selected only the genes that had a high *Z* score ($Z > 1.5$, 48 top genes) to reduce the gene expression space to those that were detected to be bimodally expressed. In this subspace, we performed hierarchical clustering, and found that cells belonging to the same cell identity clustered together (Figure S3A). The cells from human and mouse were intermixed. Further, we annotated the cell types using marker gene expressions. We found that except neural progenitor cell type and mature somites, all cell types identified in the human dataset were present in the mouse tail bud. The absence of neural progenitors and mature somites in the mouse dataset was because these tissues are more anterior to the tail bud both in the embryo and in our organoids, therefore tail bud explant used for the single cell RNA sequencing did not contain these tissues in mouse. To visualize the cell types, we performed principal component analysis and plotted the cells in the first two principal component subspace (Figure S3B).

Later, we isolated the cells belong to common cell types between these two datasets, namely Neuromesodermal Progenitors, Presomitic Mesoderm, Early Somite and Pre-Neural Tube. We looked for the highly differentially expressed genes in each cell type compared to the other cell types (Figure S3C). By plotting the mouse and human cells in each cell type separately, we saw that the marker gene expressions were similar between these two species, validating that the mouse equivalent cell types of the cells in our organoids are present in mouse embryos (Figure S3D).

We observed that the marker genes for NMP's are found to be mostly signaling molecules, consistent with the fact that NMP's are the signaling center that drives axial elongation and anteroposterior patterning.[60] Therefore, we found the highly expressed FGF and WNT ligands in NMP's for both human and mouse cells and compared them to the other tissues. This analysis showed that WNT3A is specifically expressed in neuromesodermal progenitors and presomitic mesoderm cells in both human and mouse cells (Figure S3E), which also explains the absence of canonical WNT ligands in the organoids of our companion paper[25] due to the absence of NMP's and presomitic mesoderm cells.

Simulations

For illustration, we posited a straightforward mathematical model based on our measurements to demonstrate how gradients of the diffusive FGF signals can drive anteriorly moving oscillations along the PSM. Most biochemical parameters are not known for human cells, so a detailed model is impossible. We extracted effective parameters for our model from our experiments and again emphasize that this model is for illustrating the idea and showing how simple models based on our assumptions show qualitatively similar dynamic behaviors to the organoids.

Our simulation consisted of $n = 110$ cells initially, arranged along a line in one dimension. Each cell was 5 μm long. Thus, we set the initial length of the undifferentiated PSM tissue to be 550 μm long. We assumed that each cell had an internal oscillator with a base period of 300 min based on the experimentally measured period at the most anterior end of the PSM. Based on our experimental observation, the internal oscillator was assumed to be accelerated by the cell's FGF activity (Figures 5G and S6G). We assumed FGF profile is a function of distance from the posterior tip, x:

$$FGF(x) = FGF_0\left(1 - \exp\left(-\frac{x}{l_{FGF}}\right)\right)$$

where $l_{FGF} = 300\mu m$, estimated by dpERK measurements in Figure S2M. Here FGF_0 was used to define a dimensionless variable and set it to the maximum level of $FGF(x)$.

Next we defined a short range retinoic acid signaling, described by the function:

$$RA(x') = RA_0\, exp\left(-\frac{x'}{l_{RA}}\right)$$

where x' is the distance of a cell with presomitic mesoderm identity from the somite determination front, since retinoic acid is produced by somite cells, where RA_0 is a dimensionless variable and was set to 100, and l_{RA} was set to. Given that retinoic acid inhibits FGF activity,[49,61] we modified the FGF profile with an inhibitory retinoic acid term to define the FGF activity. Therefore FGF activity at a distance from posterior tip, x, and from the somites, x', is defined as:

$$FGF_{activity} = \frac{FGF(x)}{RA(x')+1}$$

By using the measured FGF activity profile along the A-P axis (from Figure S2M) and the measured frequency profile along the same axis (Figure 3E), we inferred the function that maps the frequency of oscillation as a function of FGF activation:

$$\omega(FGF) = 1.391 - 2.619 * exp(-14.94 * FGF/FGF_0)\ rad/hr$$

We modeled the growth of the organoid by cell division at the posterior tip. In the simplest model, we assumed this division rate to be constant and set it to 2.28 divisions an hour by using the measured growth rate in Figure 4A. Below a threshold activity level of FGF, we postulated that the presomitic mesoderm would differentiate into somite cells. We calculated this activity level by using the FGF activity profile function, and the mean length of the presomitic mesoderm measured in Figure 4B and set to be $FGF_{diff} = 0.08 * FGF_0$. Cells in the model that passed this FGF threshold became somite and started expressing MESP2 when their internal oscillation phase was between $(0,\pi/2)$. This assumption was to model the activation of HES7 and MESP2 simultaneously since both are the NOTCH pathway target genes.[47]

External activation of the FGF pathway simulated by the FGF ligand was incorporated into the model by making the FGF activation along the entire PSM uniform and set to the maximum observed activation level, FGF_0.

Using these assumptions, we simulated the model using MATLAB. We set the initial phase of the internal oscillator to zero, therefore initial oscillations were synchronous. Over time, we observed a growing organoid with anteriorly traveling oscillations and a posteriorly moving somite determination front consistent with the experiments (Figure 5H). When we stimulated this model with uniform FGF profile by setting $FGF(x) = FGF_0$ at $t = 25\ h$, the entire PSM oscillated in synchrony as observed in the experiment (data not shown), and the determination front slowed down (Figure 5H), consistent with the experiment (Figure 4G). In accordance with the two-phase model,[62,63] while unperturbed control organoid, in which there are traveling HES7 waves, showed alternating MESP2 expression in a single somite segment, addition of FGF4 disrupted this alternating expression (data not shown), due to synchronous HES7 oscillations.

QUANTIFICATION AND STATISTICAL ANALYSIS

Analysis of time-lapse imaging data and generation of kymographs

Organoids were segmented using Ilastik on the phase contrast images. Fluorescence images were corrected for nonuniform illumination and autofluorescence of the media was subtracted by calculating the mean signal of the empty area for each image. Segmented organoids were rotated on the major axis and fixed on the posterior end. Signal for each pixel on the anteroposterior axis was calculated by averaging all the pixel values on the line perpendicular to the major axis on the respective position. Kymographs for HES7 and MESP2 signal were generated by using the calculated signal on the anteroposterior axis for each timepoint. For amplitude, phase, and frequency analysis, see "quantification of phase and frequency profile on anteroposterior axis and amplitude of oscillations" section.

Length fold change was calculated by finding the length of the major axis of each organoid and dividing them to their initial length. The length of the somitic mesoderm of each organoid was calculated by manually thresholding and binarizing each MESP2 kymograph and calculating the length of the line on the space axis corresponding to each timepoint on the binarized kymograph.

The length of the PSM is calculated by finding the distance from the posterior end to the position, of somite determination front, which is the most posterior position of the somitic mesoderm on the major axis. Fold change of the PSM length was calculated by dividing the PSM length at each time point by the initial PSM length for each organoid.

Segment sizes were calculated using the length of the somitic mesoderm. First, the change in the length of the somitic mesoderm between each timepoint was calculated. The timepoints corresponding to the troughs of the somitic mesoderm length change was detected. The difference of the length of the somitic mesoderm between troughs was calculated as segment sizes.

Please cite this article in press as: Yaman and Ramanathan, Controlling human organoid symmetry breaking reveals signaling gradients drive segmentation clock waves, Cell (2023), https://doi.org/10.1016/j.cell.2022.12.042

Quantification of phase and frequency profile on anteroposterior axis and amplitude of oscillations

For phase analysis, first oscillating region of each organoid was detected using HES7 kymographs by calculating the frequency with highest amplitude of the Fourier transform of the time series of each position on the anteroposterior axis. Positions with peaks between 0.21 and 0.24 h^{-1} were considered to be oscillating around the segmentation clock frequency. After cropping the oscillating region from kymographs, we used Hilbert transform following a detrending and local renormalization algorithm, following a similar approach to a previously published algorithm.[64] First, a moving average filter was applied on the space axis of kymographs with 26.66 μm window. To subtract the trend in the time axis, a moving average filter with a 6-h window was applied to the kymograph and the resulting kymograph was subtracted from the original. The time series for each anteroposterior position was then divided by a SD filter with a 6-h window. Later, phase of each position was obtained by using Hilbert transform on the time series between 38 and 43 h of the time lapse, corresponding to fourth oscillation after the small molecule perturbations. For calculating the frequency profile on the anteroposterior axis, the change in the phase was calculated between consecutive timepoints for each position during the time-lapse, and the period was calculated using this value. The position is calculated from the anterior tip (see Methods S1).

The amplitude of the oscillations was calculated using the detrended kymographs. The mean signal was calculated for the posterior part of each organoid, corresponding between 26 and 133 μm region from the posterior end. Peaks of the oscillations after the small molecule perturbations was detected. The signal of the fourth peak following the perturbation was normalized by the signal of the first peak following the perturbation.

Supplemental figures

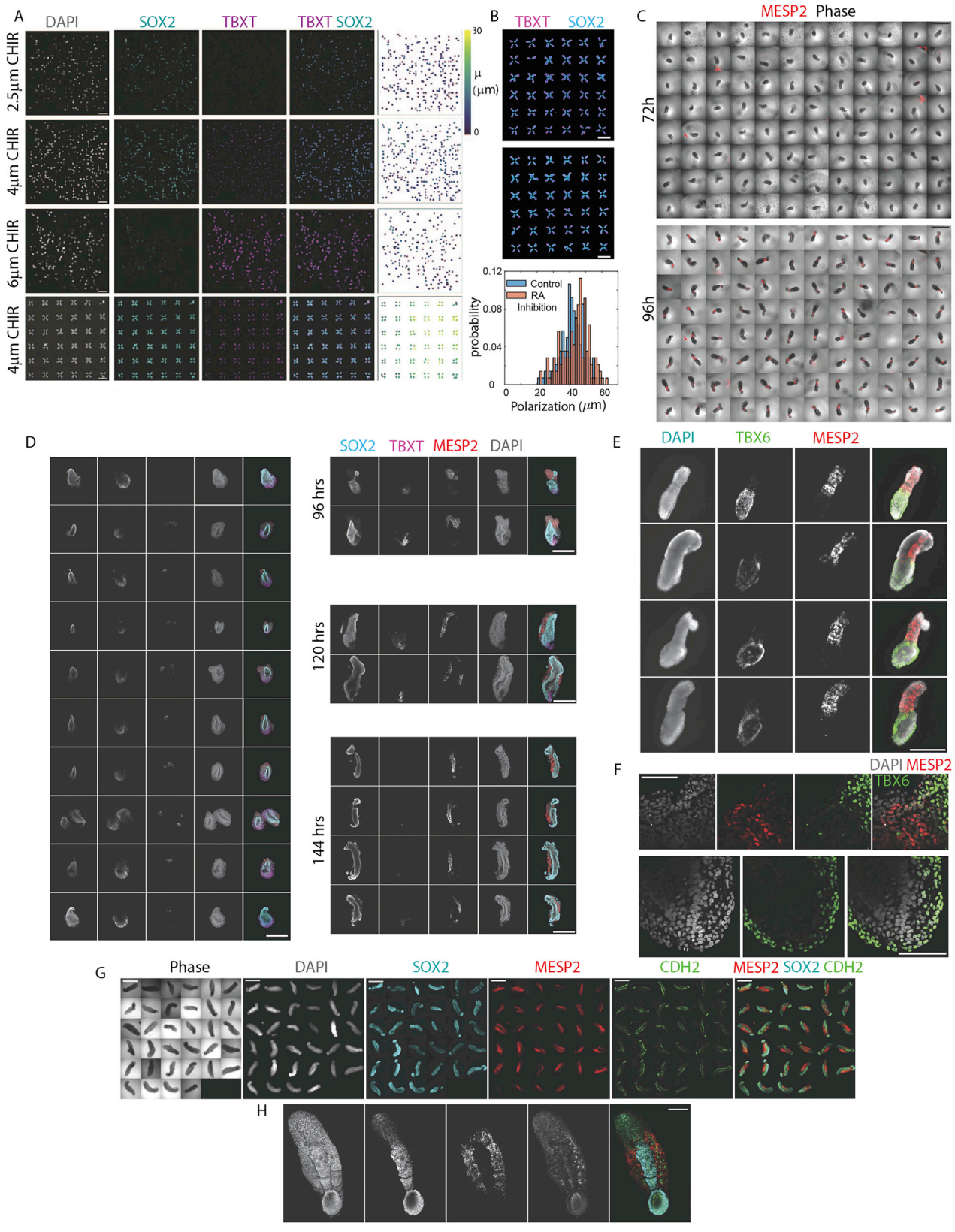

(legend on next page)

Figure S1. Elongating axial organoids generates neural tube with a single lumen flanked anteriorly by segmented somites and posteriorly by presomitic mesoderm, related to Figure 1

(A) Randomly positioned organoids (top three rows) and micropatterned organoids (bottom row) in groups of four on the vertices of a square on a coverslip, each consisting of a single epithelial layer of cells enclosing a single lumen, treated with BMP inhibitor LDN193189 (0.5μM), TGFβ inhibitor A83-10 (0.5μM) and WNT agonist CHIR99021 (top to bottom: 2.5μM, 4μM, 6μM, 4 μM) for 48 h stained for DAPI, SOX2 and TBXT. Organoids were segmented based on DAPI signal. Rightmost column shows each organoid's position on the respective row colored by their dipole moment. Scale bar, 1mm.

(B) Micropatterned organoids in groups of four on the vertices of a square on coverslips under normal differentiation conditions (LDN193189 (0.5μM), A83-10 (0.5μM) and CHIR99021 (4 μM)) for 48 h (top) or in addition treated with the retinoic acid inhibitor AGN193109 (1 μM) for 48 h (middle) stained for SOX2 and TBXT. Normalized histograms of dipole moments for control organoids and organoids with AGN193109 treated organoids (bottom). Retinoic acid inhibition does not affect polarization of organoids. Scale bars, 1 mm.

(C) Phase contrast images overlayed with MESP2::mCherry signal in live organoids in a 96-well low adhesion plate at 72 h (top) and 96 h (bottom) of differentiation. Scale bars, 1 mm.

(D) Confocal sections of representative organoids with MESP2::mCherry reporter on consecutive days of differentiation (72 h, 96 h, 120 h, 144 h) stained for SOX2, TBXT. SOX2 and TBXT co-expressing NMP's reside at the posterior tip. Scale bars, 500 μm.

(E) Epifluorescence image of organoids with MESP2:mCherry reporter stained for paraxial mesoderm marker TBX6 at 120h of differentiation. Scale bars: 500μm.

(F) Confocal sections of an organoid from with MESP2::mCherry reporter from (top) determination front and (bottom) posterior tip at 120 h of differentiation stained for TBX6. TBX6 and MESP2 expressing cells forms a clear boundary at the determination front. Scale bars, 100 μm.

(G) Epifluorescence image of organoids with MESP2:mCherry reporter stained for neural marker SOX2 and N-Cadherin (CDH2) which is condensed at the apical side of epithelial cells. All organoids have a neural tube flanked by segmented epithelialized somites. Scale bars, 1 mm.

(H) Maximum intensity projection from confocal sections of an organoid with MESP2::mCherry reporter stained for neural marker SOX2 and N-Cadherin (CDH2). Scale bars, 200μm.

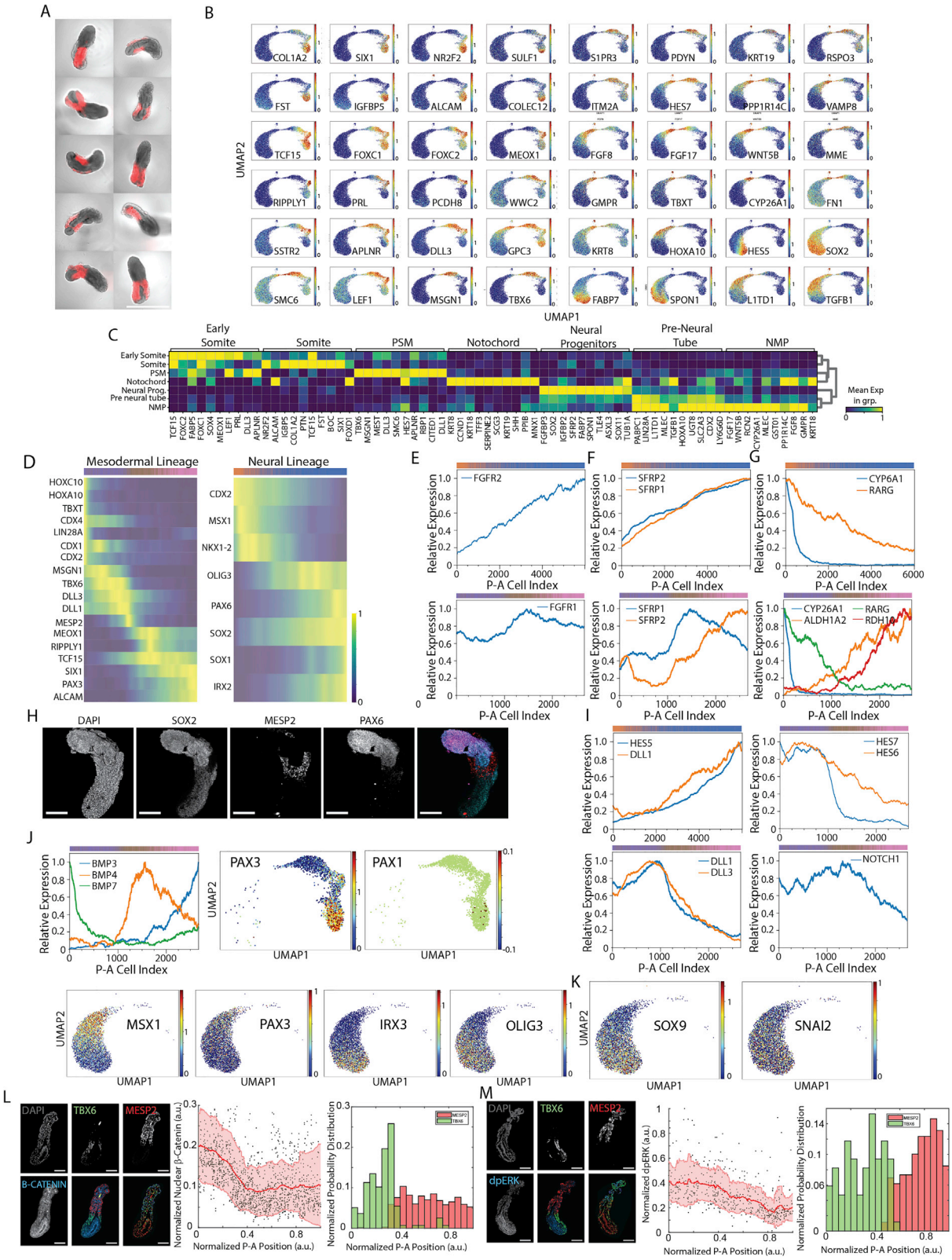

(legend on next page)

Figure S2. Anteroposterior organization of cell types and gene expression profiles inferred from single cell RNA-seq, related to Figure 2

(A) Epifluorescence image of organoids with MESP2:mCherry reporter at 120h of differentiation. We performed single-cell RNA sequencing of 11009 cells obtained from these organoids after dissociation and pooling. Scale bar: 1 mm.

(B) UMAP (uniform manifold approximation and projection) plots showing the log-normalized gene expression values of the genes identified by SMD.

(C) Heatmap of top 10 differentially expressed genes with highest fold change for each cell type compared to the other cell types. Genes are colored by their normalized mean expression in the respective cell type. Normalization is done by scaling log-normalized expression of each gene between 0 and 1.

(D) Heatmap of top key genes (y axis) for mesodermal (left) cell clusters (presomitic mesoderm, early somite, and somite) and neural (right) cell clusters (pre-neural tube and neural progenitors) in cells (x axis) ordered according to their inferred anteroposterior positions. Genes are ordered based on the position of their peak expression on the inferred A-P axis. Color bars on the top of heatmaps represent the cluster identity of the individual cells (same color code as in Figure 2A).

(E) Normalized posterior-anterior gene expression profiles for FGFR2 in neural clusters (top), FGFR1 in mesodermal clusters (bottom).

(F) Normalized posterior-anterior gene expression profiles for secreted WNT pathway inhibitors, SFRPs in neural (top) and mesodermal (bottom) clusters. SFRP's show high expression in the anterior for both neural and mesodermal clusters. Color bars on the top of plots represent the cluster identity of the individual cells (same color code as in Figure 2A).

(G) Normalized posterior-anterior gene expression profiles for RA pathway related genes in neural clusters (top) and mesodermal clusters (bottom).

(H) Confocal sections of an organoid with MESP2::mCherry reporter on 120 h of differentiation stained for SOX2 and PAX6. PAX6 expression is upregulated anterior to the determination front. Scale bar, 200 μm.

(I) Normalized posterior-anterior gene expression profiles for NOTCH target HES5 and NOTCH ligand DLL1 in neural clusters (top left); NOTCH targets (top right), NOTCH ligands (bottom left) and NOTCH receptor (bottom right) in mesodermal clusters. Color bars on the top of plots represent the cluster identity of the individual cells (same color code as in Figure 2A).

(J) (Top left) Normalized posterior-anterior gene expression profiles for BMP ligands expressed in the mesodermal clusters. Color bars on the top of plots represent the cluster identity of the individual cells (same color code as in Figure 2A). UMAP plots showing the log-normalized gene expression values of the genes associated with dorsal (PAX3, MSX1, IRX3, OLIG3) and ventral (PAX1) cell identities.

(K) UMAP plots showing the log-normalized gene expression values of neural crest markers SOX9 and SNAI2 on neural cell clusters.

(L) Confocal sections of an organoid with MESP2::mCherry reporter stained for TBX6 and β-catenin. Nuclei were segmented based on DAPI signal and colored based on the mean nuclear β-catenin signal (left panel, bottom right). Scale bar, 200 μm. Plot of nuclear β-catenin signal along the anteroposterior axis (middle panel). Each black dot represents a nucleus. Solid line: mean, shaded area: SD around mean. Plot of the distribution of TBX6+ (green) and MESP2+ (red) cells on anteroposterior axis for the organoid in the left panel (right panel).

(M) Confocal sections of an organoid with MESP2::mCherry reporter stained for TBX6 and doubly phosphorylated ERK (dpERK). Nuclei were segmented based on DAPI signal and colored based on the mean nuclear dpERK signal (left panel, bottom right). Scale bar, 200 μm. Plot of nuclear dpERK signal along the anteroposterior axis (middle panel). Each black dot represents a nucleus. Solid line: mean, shaded area: SD around mean. Plot of the distribution of TBX6+ (green) and MESP2+ (red) cells on anteroposterior axis for the organoid on the left panel (right panel).

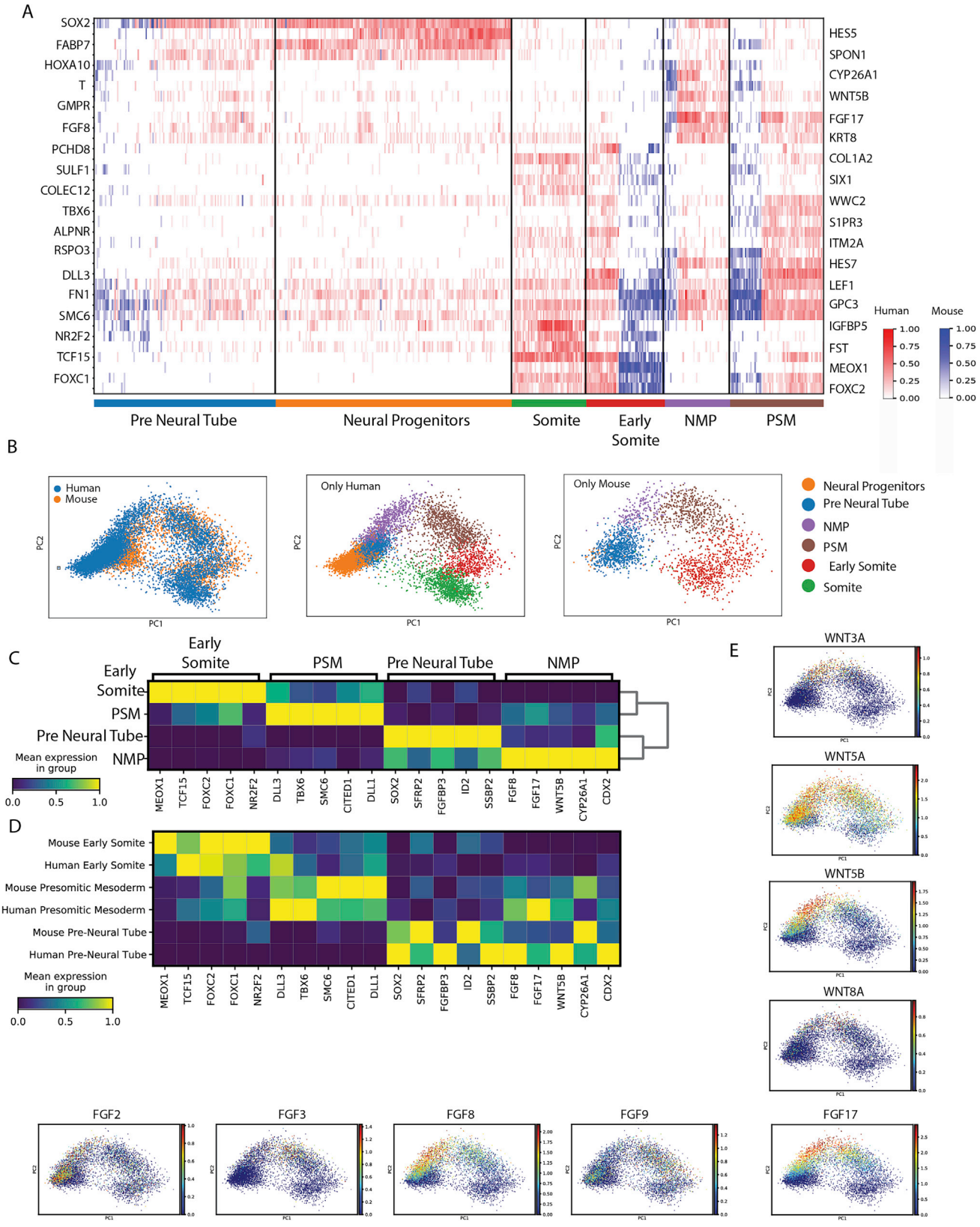

(legend on next page)

Figure S3. Comparison of cell types with *in vivo* mouse cells, related to Figure 2

(A) Heatmap of cell-gene matrix of human and mouse combined dataset hierarchically clustered in the high *Z* score gene subspace. Blue cells: Mouse, Red cells: Human. Cell clusters are annotated by the marker gene expressions.

(B) Distribution of human and mouse cells in the first two principal component of high *Z* score gene subspace. Top left: Cells are colored by species. Top right: Only human cells are shown, colored by cell identity. Bottom: Only mouse cells are shown, colored by cell identity.

(C and D) Matrix plot showing the marker gene expression levels for (C) cell clusters containing both human and mouse cells and (D) cell clusters containing only human or only mouse cells.

(E) PCA plots showing the log-normalized gene expression values of the FGF and WNT ligands highly expressed by neuromesodermal progenitor cells.

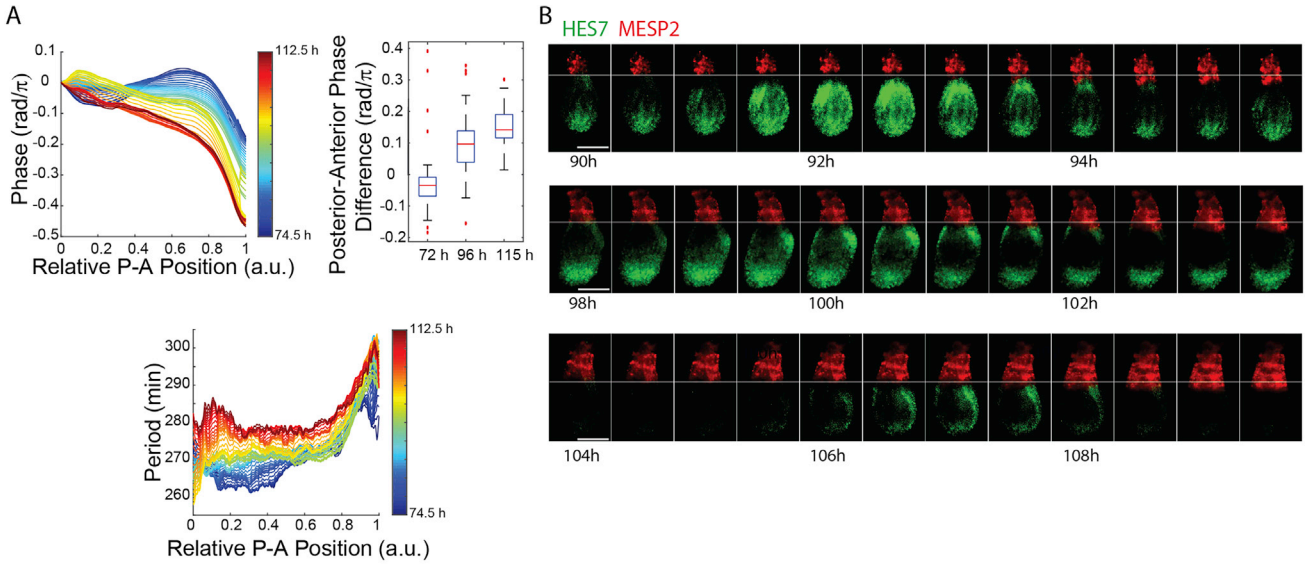

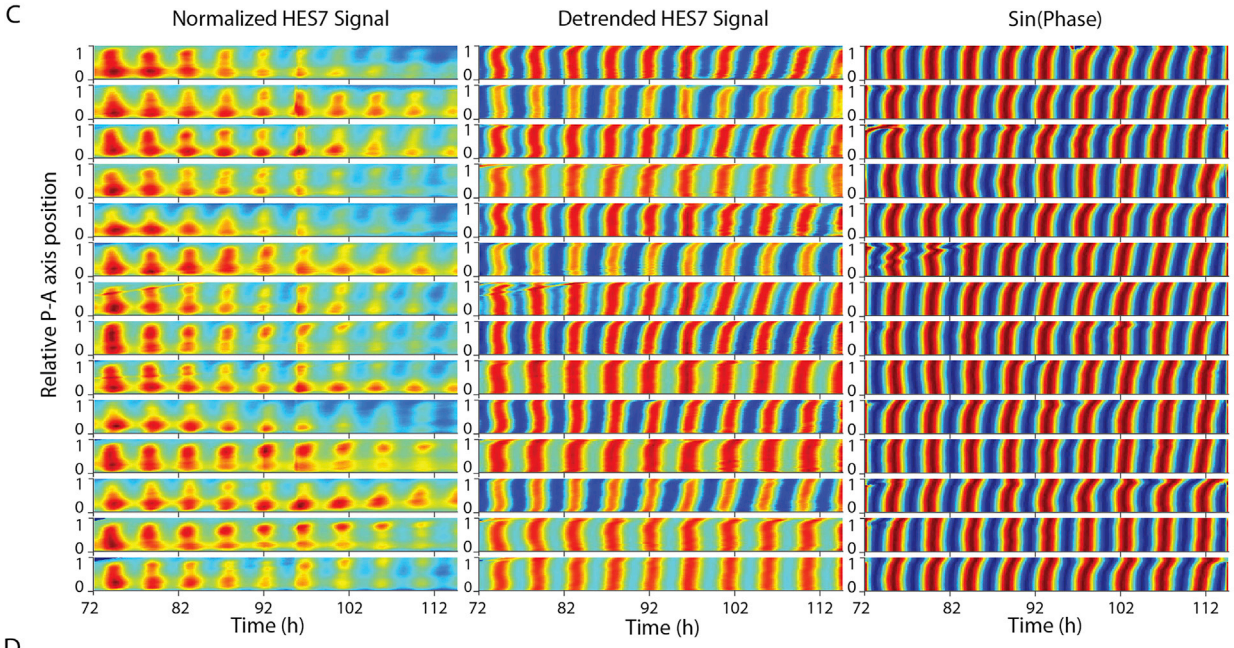

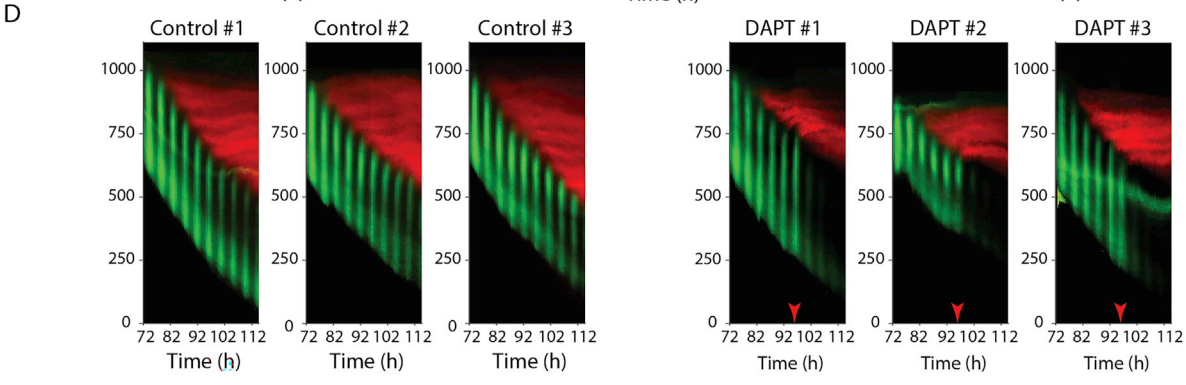

(legend on next page)

Figure S4. Dynamics of somitogenesis and NOTCH gene expression waves in the organoids, related to Figure 3

(A) (top left) Plot showing the time evolution of anteroposterior phase profile of the organoids in basal media, averaged over n = 53 organoids between t = 74.5 h and t = 94 h, and n = 14 organoids between t = 94 h and t = 112.5 h. Lines are colored by their corresponding time point. (top right) Boxplot of the phase difference between posterior and anterior half of the organoids on 72h (n = 53), 96h (n = 53) and 115h (n = 14) of differentiation. Center line, median; box, interquartile range; whiskers, range not including outliers; '+' marker symbols: outliers. (bottom) Plot showing the time evolution of anteroposterior phase profile of the organoids in basal media, averaged over n = 14 biologically independent organoids. Lines are colored by their corresponding time point.

(B) Stills from time-lapse imaging of three biologically independent organoids with HES7 (green) and MESP2 (red) expression reporters. Shaded line shows the position of the determination front at the first timepoint for each organoid. A new segment of MESP2 expression appears when each HES7 wave reaches to the determination front. Time interval between consecutive images is 30 min. Scale bars, 200 μm.

(C) Kymographs of normalized HES7 signal (left), detrended HES7 signal (middle) and sine of the detected instantaneous phase of the oscillations for 14 organoids along the anteroposterior axis of organoids from 72 h to 114.75 h of differentiation. These kymographs were used to calculate the phase profile of Control organoids in Figure 3E. Data collected every 15 min. For normalization, detrending of the signal and phase detection, see STAR Methods.

(D) Kymographs showing the dynamics of HES7 (green) and MESP2 (red) expression along the anteroposterior axis of organoids from 72 h to 114.75 h of differentiation for three control organoids (left) and three organoids treated with DAPT (25 μM) at 95h (right). Data collected every 15 min for all plots.

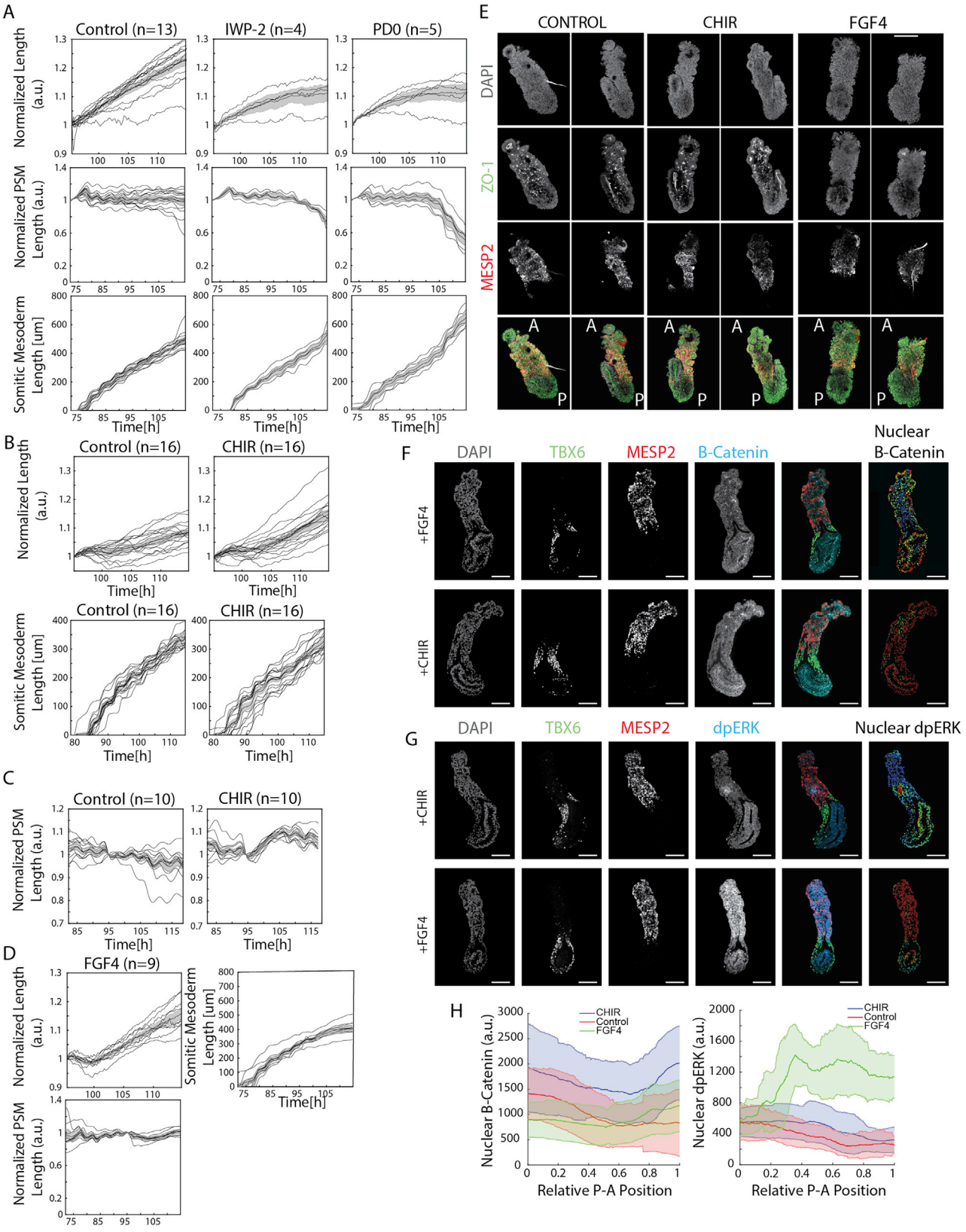

(legend on next page)

Figure S5. FGF drives somite determination front propagation and somite segmentation while WNT drives axial elongation, related to Figure 4

(A) Plots of length fold change (top row), presomitic mesoderm length fold change (middle row) and somitic mesoderm length (bottom row) of organoids treated with PD0325901 (1μM, n = 5, right column), IWP-2 (2μM, n = 4, middle column) and unperturbed control (n = 13, left column) over time. PD0325901 and IWP-2 was administered at 95.5 h for the perturbed organoids. Solid lines represent individual organoids, shaded area: SE around mean.

(B) Plots of length fold change (top row), and somitic mesoderm length (bottom row) of organoids treated with CHIR (3μM, n = 16, right column) unperturbed control (n = 16, left column) over time. CHIR was administered at 95.5 h for the perturbed organoids. Solid lines represent individual organoids, shaded area: SE around mean.

(C) Plot showing presomitic mesoderm length fold change of organoids treated with CHIR (3μM, n = 10, right) unperturbed control (n = 10, left) over time. CHIR was administered at 95.5 h for the perturbed organoids. Solid lines represent individual organoids, shaded area: SE around mean.

(D) Plots of length fold change (top left), presomitic mesoderm length fold change (bottom) and somitic mesoderm length (top right) of organoids treated with FGF4 (100 ng/mL, n = 9) over time. FGF4 was administered at 95.5 h for the perturbed organoids. Solid lines represent individual organoids, shaded area: SE around mean.

(E) Confocal images of control (first two columns from left) CHIR treated (third and fourth column from left) and FGF4 treated (last two column from left) organoids at 120 h of differentiation stained for DAPI, epithelial marker ZO-1 and somite marker MESP2. Scale bar, 200μm.

(F) Confocal sections of an organoid with MESP2::mCherry reporter, treated with FGF4 (100 ng/mL, top row) and CHIR (3μM, bottom row) for 4.5 h, stained for TBX6 and β-catenin. Nuclei were segmented based on DAPI signal and colored based on the mean nuclear β-catenin signal (rightmost column). Scale bar, 200 μm.

(G) Confocal sections of an organoid with MESP2::mCherry reporter, treated with FGF4 (100 ng/mL, bottom row) and CHIR (3μM, top row) for 4.5 h, stained for TBX6 and doubly phosphorylated ERK (dpERK). Nuclei were segmented based on DAPI signal and colored based on the mean nuclear dpERK signal (rightmost column). Scale bar, 200 μm.

(H) Plots of nuclear β-catenin signal (left) and nuclear dpERK signal (right) along the anteroposterior axis of organoids treated with FGF4 (100 ng/mL, green) and CHIR (3μM, blue) for 4.5 h, and unperturbed control organoids (red). Solid lines: mean, shaded areas: SD around mean.

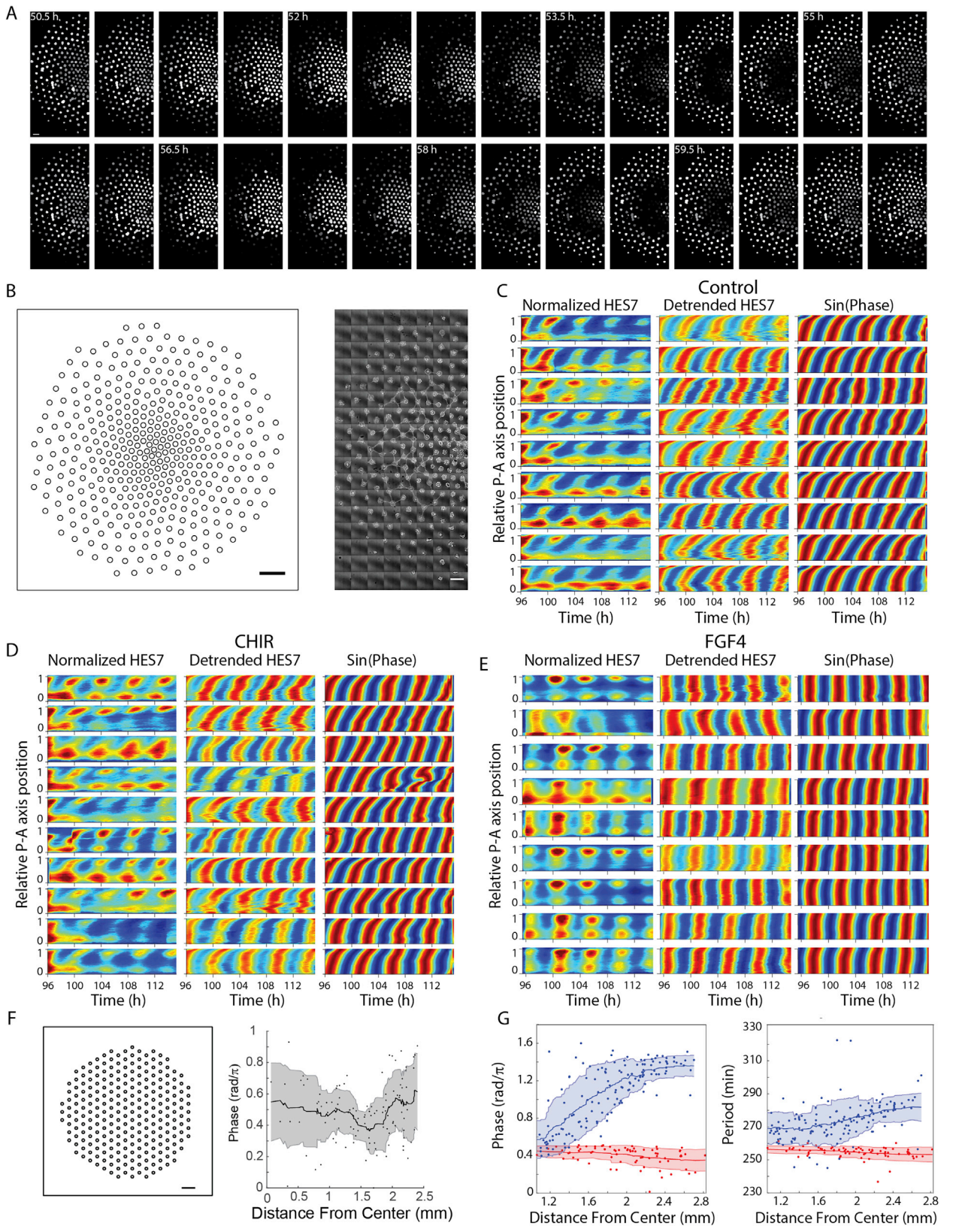

(legend on next page)

Figure S6. FGF gradient is required for HES7 traveling expression waves and somite segmentation, related to Figure 5

(A) Stills from time-lapse imaging PSM colonies on microcontact printed arrays with HES7 expression reporter. Detrended HES7 signal averaged over each colony is represented by color intensity. Scale bar, 500 μm.

(B) Left: Outline of the whole microcontact printed array. Each circle represents a colony. Scale bar, 1mm. Right: Phase contrast image of the microcontact printed colonies at 48 h of differentiation. Scale bar, 500 μm.

(C–E) Kymographs of normalized HES7 signal (left), detrended HES7 signal (middle) and sine of the detected instantaneous phase of the oscillations for 9 unperturbed organoids (C) 10 organoids treated with CHIR (D) and 9 organoids treated with FGF4 (E) along the anteroposterior axis of organoids. Kymographs in (C) and (D) were used to calculate the phase profile of Control and CHIR treated organoids in Figure 5F, right, respectively. Kymographs in (E) were used to calculate the phase profile of FGF4 treated organoids in Figure 5F, left. Data collected every 15 min.

(F) Left: Outline of the whole microcontact printed array with uniformly spaced colonies. Each circle represents a colony. Scale bar, 1mm. Right: Plots showing oscillation phase of each colony in the uniformly spaced colony array and its distance from the center of the array Dots represent individual colonies, lines represent mean and shaded areas represent SD.

(G) Plots showing oscillation phase (left) and period (right) of each colony and its distance from the center of the array for the arrays treated with FGF4 (red) and the unperturbed control (blue). Dots represent individual colonies; lines represent mean and shaded areas represent SD. Period difference between r = 1.2 mm and r = 2.5 mm is found to be 7.5 ± 15.8 min, which is %2.8 ± 5.8 of one period of oscillation. Therefore, the measured period difference is insignificant in terms of traveling waves.